

Improving the Characteristics of Expansive Soil Using Coarse-grained Soil

Sherif M. ElKholy

**Department of Civil Engineering, College of Engineering
Qassim University, Qassim, Kingdom of Saudi Arabia, selkholy@qec.edu.sa
On leave from: Construction Research Institute, National Water Research Center
Cairo, Egypt**

(Received 2/1/2008; accepted for publication 4/6/2008)

Abstract

Expansive soil covers many areas in the world, especially the arid and semi-arid regions. In Saudi Arabia, there are several areas where this kind of problematic soil exists in the form of variable-thicknesses layers in the developed regions. For everyday construction activities various precautions have to be considered in order to minimize the risk of construction on such a soil. Geotechnical researchers have proposed several measures in order to improve the properties of expansive soil. These measures utilize one of two techniques, either the full replacements of these expansive soil layers or the treatment of expansive soil with a wide range of additives. In the current study, a new measure of treating the expansive soil is proposed in order to improve its expansion characteristics. The treatment measure is based on mixing the expansive soil with coarse-grained soil with special gradation. The swelling tests conducted on this mixture resulted in drastically reducing the swelling indices such as swelling pressure, swelling potential and swelling index. Additionally some empirical correlations are proposed to relate the expansion indices with the percentage of the coarse-grained fraction of the expansive soil.

Keywords: Expansive soil, swelling potential, swelling index, swelling pressure, coarse fraction.

1. Introduction

Expansive soil is one of the problematic soils that face many geotechnical engineers in the field (others include collapsible soil, quick clays.....etc). The expansive soil is known to cause sever damage to structures that are founded on it. In Saudi Arabia, there is no confirmed information about the economic losses due to structures founded on expansive soils. However, there are several well-documented cases of structural damage spread throughout many areas of Saudi Arabia [1]. The reported cases include structural damage of some buildings in Al-Ghatt City near Riyadh and Mobaraz town in the eastern region and some road and earth embankments damages in the eastern region where the sub-grade layers were constructed over expansive soil. It was also reported that it is estimated that economic losses in Saudi Arabia during the period 1977-1987 totaled about 300 million US dollars [1]. Safe and economic designs of foundations on expansive soils require determining the swelling indices such as swelling pressure, swelling potential and swelling index. These indices are typically determined in all geotechnical laboratories.

In literature, there are reports of plenty of structural damage cases due to construction on expansive soils [2]. [3], [4], especially for water and irrigation structures due to pore water seeping through embankments constructed over expansive soil layers. Therefore, researchers have been trying to investigate the proper measures that could be taken to reduce the expected structural damage. Researchers have been adopting the technique of treatment of expansive soil with additives in order to increase the shear strength of expansive soil after saturation and consequently reducing the soil heaving and its swelling pressure. Katti [5] showed that using a cohesive non-swelling soil caution, of adequate thickness, on top of the expansive soil layer, underneath the foundation, is effective in improving the swelling characteristics of expansive soil. Byer [6] concluded that using a compacted expansive soil-lime mixture (4% granular quicklime) caution may overcome the cracking and sliding of the side slopes lining of the Friant-Kern canal in California, USA. The Government of Karnatak, India used a 1.0 m layer of cohesive non-swelling soil to line the bed and side slopes of a canal constructed in a black cotton soil deposits. It was concluded that this caution helped in retaining considerable shear strength of the black cotton soil after saturation. Sorochan [7] recommended adopting the technique of using soil replacement cautions in stabilization of beds and side

slopes of waterways constructed in expansive soil deposits. He reported that the soil cautions might consist of loams, sandy loams, non-expansive clays, and in certain case sands or sand-gravel mixes. Sorochan [7] reported that these cautions reduced the non-uniform heave of expansive soil. Marei et al. [8] conducted an experimental study to investigate the effect of using different types of cautions on the behavior of expansive soil. They concluded that using the replacement non-swelling caution significantly reduced the swelling potential and the swelling pressure. The sand-lime mix caution caused the largest reduction in swelling potential and swelling pressure compared to other cautions (sand or clayey silt), which was attributed to the effect of the chemical action of lime. Marei et al. [8] concluded that the sand-lime mix caution also caused a slower rate of swelling and considerable improvement in the shear strength properties of the expansive soil.

Other researchers have been investigating the development of empirical relationships to predict the swelling characteristics based on placement conditions, dry density, initial moisture content, and Atterberg's limits, (Satyanarayana and Rangamanatham [9], Komarnik and David [10], Mallikarjuna Rao [11], Mowafy and Bauer [12], and Erzin and Erol [13]). These relationships serve in predicting quick estimates of the swelling characteristics and they may also be used to verify data collected from laboratory and field tests. These empirical relationships, however, were not found to be applicable for all kinds of soil [11]. This may be explained by the fact that the determination of Atterberg's limits utilizes only the portion of soil sample passing from sieve number 40 according to ASTM "D4318". This means that the portion of soil sample, which is coarser than 0.425 mm, may affect the resulting swelling characteristics. The current study attempts to investigate the influence of the soil sample, which is coarser than 0.425 mm on the swelling characteristics through conducting a series of laboratory tests on three sets of expansive soils collected from different sites.

2. Tested soil

Expansive soil samples collected from three different sites at the Al-Qassim region were used for the laboratory-testing program. Soil samples were collected in an undisturbed state using the open pit technique at a depth of about 5 m. The physical and engineering properties of the three soil sets were measured and the results are shown in Table (1). The soil samples are classified as CH (clay with high plasticity)

and designated as Soil (1), Soil (2), and Soil (3) as shown in Table (1). The results of the free swell and liquid limit tests reported in Table (1) show that the three soils have the potential to be highly expansive soil. The samples were then dried, pulverized and sieved through sieve number 40 and the soil portion passing through it was used in the laboratory testing program.

3. Testing program

A laboratory-testing program was designed to investigate the swelling characteristics, swelling potential, swelling pressure, and swelling index of the three soil sets. These characteristics are used as the comparison base for the soils before and after treatment in order to improve the swelling characteristics. For each of the three sets, the soil portions finer than 0.425 mm are determined and shown in Table (1). The three soils are clear of any portion of soil that is coarser than 0.425 mm. In order to investigate the improvement in the properties of expansive soils due to increasing the portion of soil that is coarser than 0.425 mm, four different mixtures are prepared from each soil type shown in Table (1).

Table (1): Properties of the three sets of soil used in the study

Properties	Soil (1)	Soil (2)	Soil (3)
Specific Gravity, G_s	2.68	2.71	2.72
% of Gravel	0	0	0
% of Sand	37	34	32
% of Silt and Clay	63	66	68
Liquid Limit	98	105	134
Plastic Limit	27	37	48
Plasticity Index	71	68	86
Free Swell Index	171	191	232
Activity	1.51	1.31	1.79
USCS Classification	CH	CH	CH

The mixtures are prepared of each soil set mixed with sandy soil coarser than 0.425 mm in percentages of 0% (before mixing), 20%, 40%, 60%, and 80% by weight. The samples are marked as: Sample (S-1), Sample (S-2), Sample (S-3), Sample (S-4), and Sample (S-5), where S indicates the tested soil type (1, 2, and 3) and the numbers 1-5 refer to the percentage of the sandy soil coarser than 0.425 mm added (0%, 20%, 40%, 60%, and 80%). Figure (1) shows the gradation of the three soils as well as the sandy soil used in the mixtures and Table (2) shows the samples mixtures used in the testing program. The Atterberg's Limits of the all sample

mixtures are similar to the original soils (Soil (1), Soil (2), and Soil (3)) since the added soil is sandy soil whose particle sizes are coarser than 0.425 mm. The sample mixtures are prepared in the oedometer cell (50 mm diameter and 20 mm thickness) and statically compacted before conducting the tests. The oedometer tests are performed on the prepared soil mixtures. The swelling characteristics, swelling pressure, swelling potential, and swelling index, are determined for the tested soil-mixture sample.

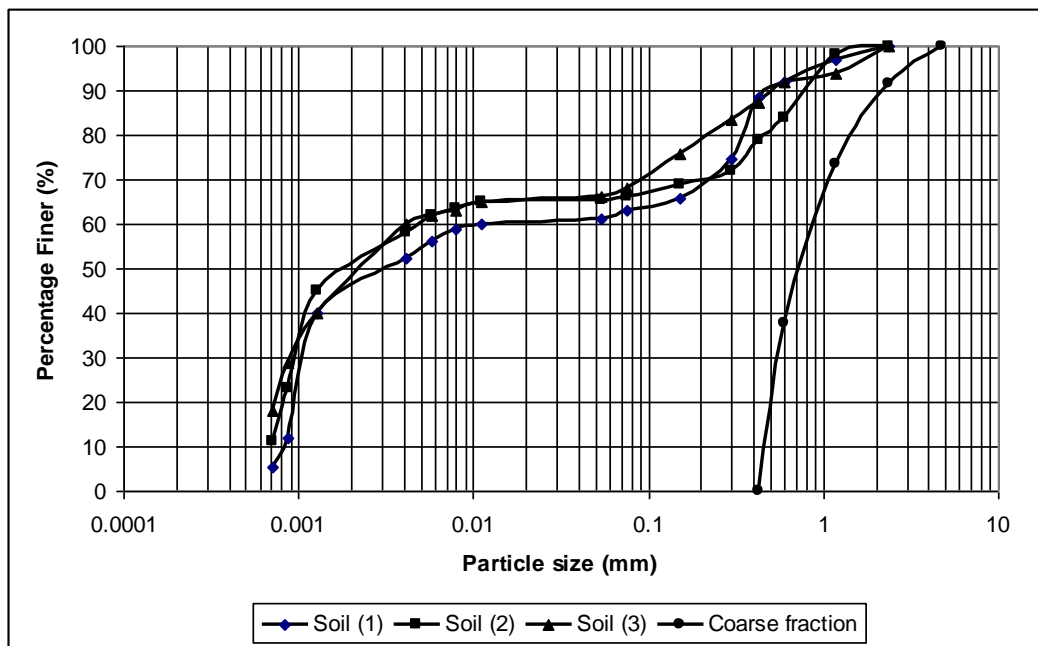


Fig. (1). The particle size gradation of the tested expansive soils and the coarse fraction sandy soil used in the mixture

Table (2). The soil mixtures used in the testing program

Sample (S-1)	Sample (S-2)	Sample (S-3)	Sample (S-4)	Sample (S-5)
100% Soil (1) + 0.0% Sand	80% Soil (1) + 20% Sand	60% Soil (1) + 40% Sand	40% Soil (1) + 60% Sand	20% Soil (1) + 80% Sand
100% Soil (2) + 0.0% Sand	80% Soil (2) + 20% Sand	60% Soil (2) + 40% Sand	40% Soil (2) + 60% Sand	20% Soil (2) + 80% Sand
100% Soil (3) + 0.0% Sand	80% Soil (3) + 20% Sand	60% Soil (3) + 40% Sand	40% Soil (3) + 60% Sand	20% Soil (3) + 80% Sand

4. Results and discussion

4.1 Oedometer test results

The results of the free swell oedometer tests on the three tested expansive soils as well as the prepared mixtures are plotted in the form of e vs $\log p$ are shown in Figures (2), (3), and (4) respectively. The plots show that adding the coarse friction sandy soil to the three expansive soils tested has significantly influenced the resulted e vs $\log p$ relationships; that is at the same applied pressure (p) the voids ratio (e) is significantly lower. The largest reduction was achieved at the largest percentage of added coarse fraction (80 %). The results and the influence on swelling characteristics are discussed in details in the following sections to show that for all three soils, the swelling characteristics decreased with different percentages depending on the percentage of the coarse fraction mixed with the swelling soil.

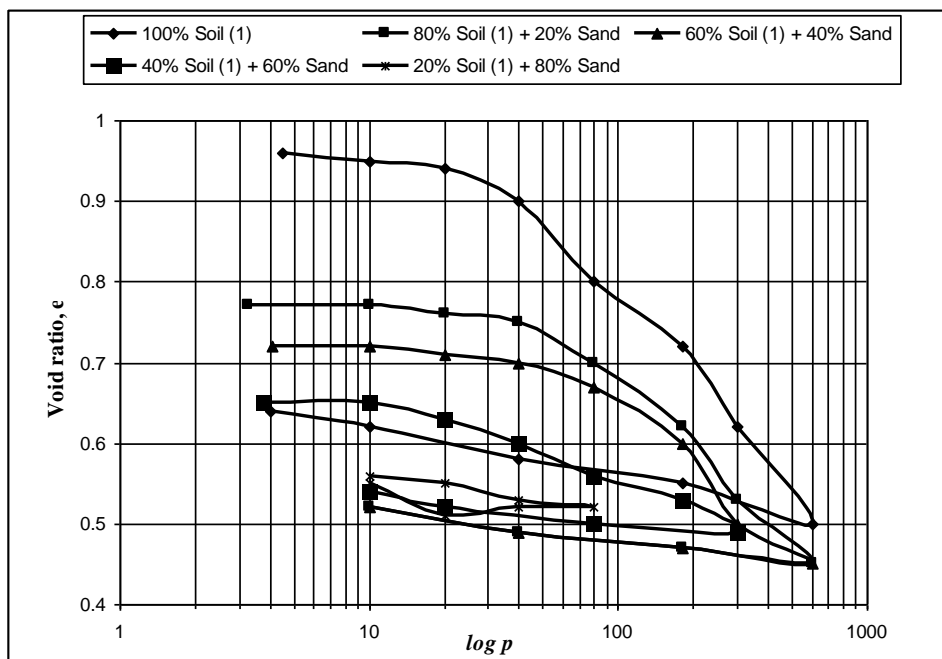


Fig. (2). The results of the free swell oedometer test for soil (1)

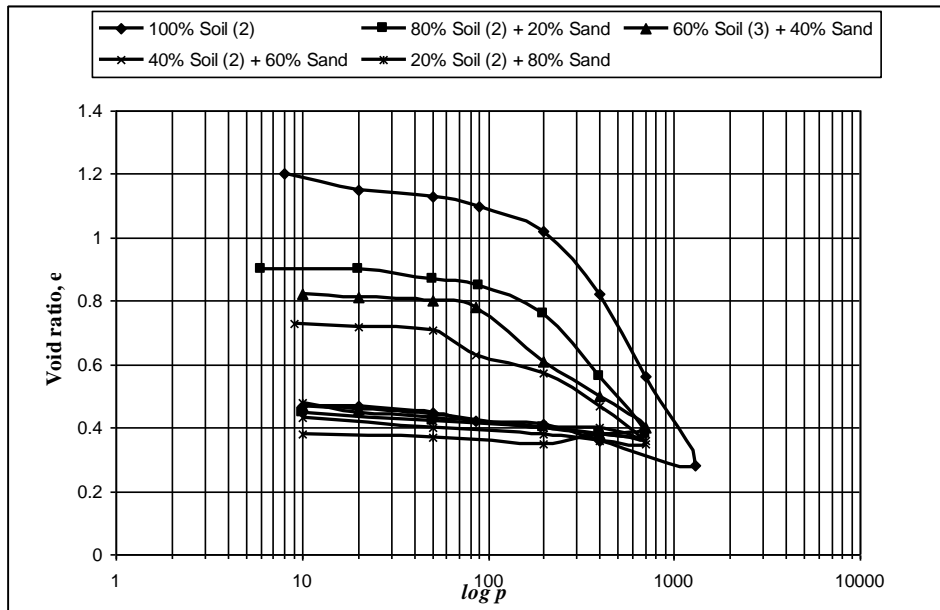


Fig. (3). The results of the free swell oedometer test for soil (2)

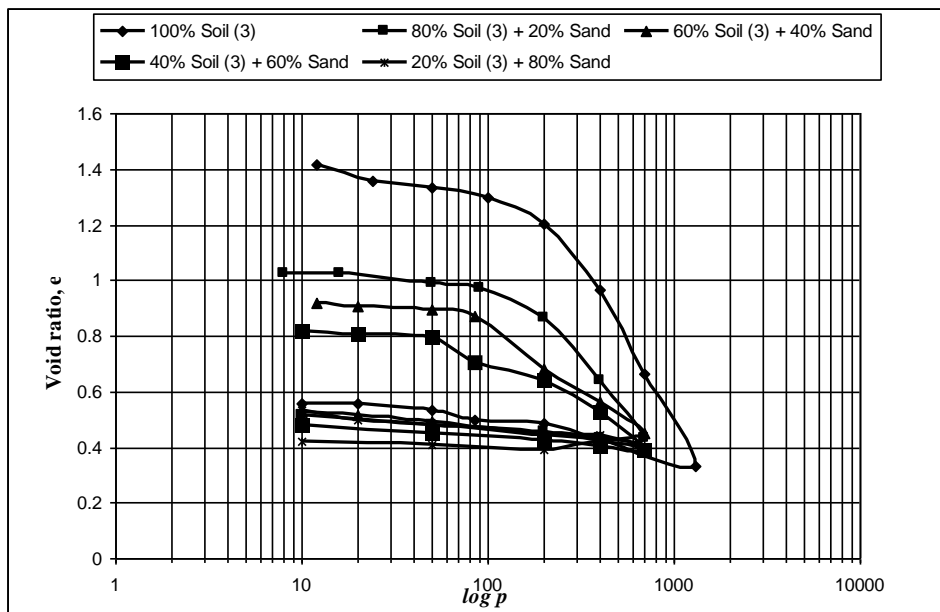


Fig. (4). The results of the free swell oedometer test for soil (3)

4.2 Swelling characteristics

The swelling characteristics in the form of swelling pressure, swelling potential and swelling index are determined for the tested expansive soils as well as the soil mixtures. The dial gauge readings of the oedometer test were recorded at intervals 0.5, 1, 2, 4, 8, 15, 30, 60, 120, and 240 minutes, then at every 24 hours time interval until full swelling occurred when the dial gauge reading is constant. The results of swelling potential, swelling pressure, and swelling index for the three soils are shown in

Figures (5), (6), and (7) respectively. The percentage of change (reduction or increase) in any swelling characteristic was evaluated by comparing its value before and after soil treatment as follows:

$$\text{Change \%} = \frac{[\text{Value (before treatment)} - \text{Value (after treatment)}]}{\text{Value (before treatment)}} \quad (1)$$

4.3.1 Swelling potential

As shown in Figure (5), an increase in the percentage of coarse fraction sand mixed with swelling soil from 0% to 80% reduced the swelling potential (SP) of the three tested soils. For Soil (1), SP decreased from 47.15% to 0.96%. For Soil (2), SP decreased from 56.45% to 1.38%. For Soil (3), SP decreased from 66.56% to 1.62%. This reduction in SP may be attributed to the presence of the coarse fraction sandy soil mixed with the swelling soil. The non-swelling nature of the coarse fraction may also counteract the process of swelling through surface friction among soil particles. Figure (8) shows the variation of the percentage of reduction in swelling potential (R-SP), evaluated using equation (1), with the percentage, by weight, of coarse fraction sand (CF) available in the expansive soil. Figure (8) also shows a best fit line between the two variables; the expected reduction percentage in SP and the percentage of coarse grained fraction in the expansive soil. The empirical equation of the best fit curve may be expressed as follows:

$$(R-SP) = 100 (1 - e^{-0.031 CF}) \quad (2)$$

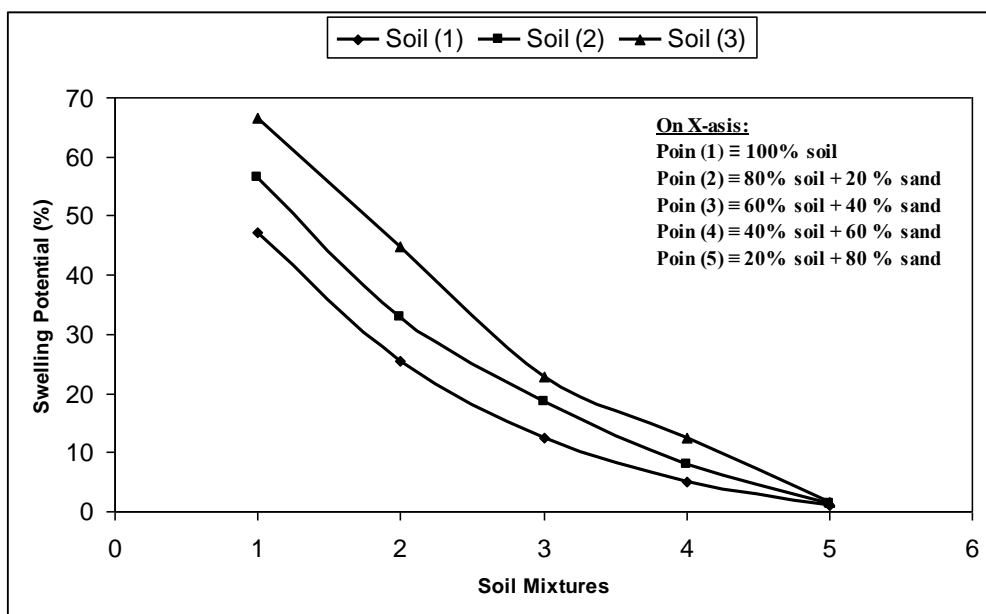


Fig. (5). The resulted swelling potential for the soil mixtures

4.3.2 Swelling pressure

As shown in Figure (6), an increase in the percentage of coarse fraction sand mixed with swelling soil from 0% to 80% reduced the swelling pressure (SPR) of the three tested soils. For Soil (1), SPR decreased from 555 to 45 kPa. For Soil (2), SPR decreased from 690 to 35 kPa. For Soil (3), SPR decreased from 880 to 70 kPa. Again, this reduction in SPR is attributed to the presence of the coarse fraction sandy soil mixed with the swelling soil. Figure (9) shows the variation of the percentage of reduction in swelling pressure (R-SPR) with the percentage, by weight, of the coarse grained fraction soil (CF) available in the expansive soil. Figure (9) also shows the best fit curve for the relationship which relates between the reduction in SPR and the percentage of coarse grained fraction available in the expansive soil. The empirical relationship may be expressed as follows:

$$(R-SPR) = 100 (1 - e^{-0.02 CF}) \quad (3)$$

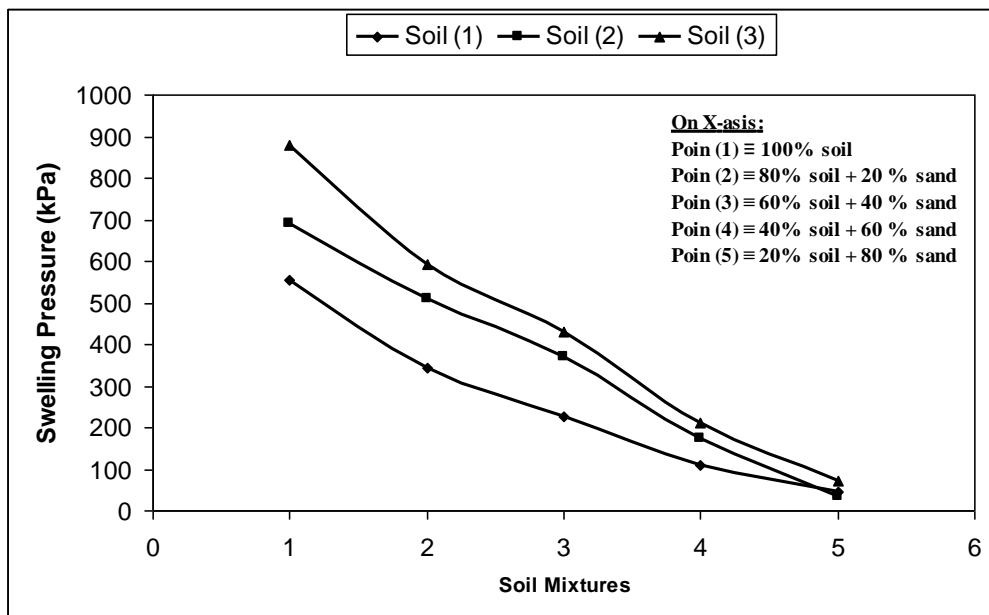


Fig. (6). The resulted swelling pressure for the soil mixtures

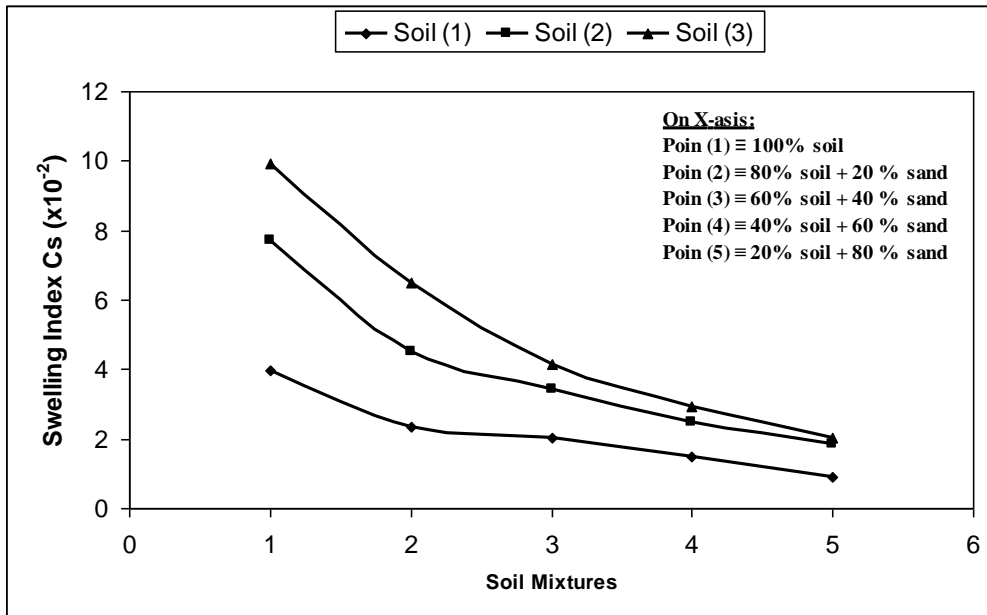


Fig. (7). The resulted swelling index for the soil mixtures

4.3 Influence of coarse fraction on swelling characteristics

4.3.3 Swelling index

As shown in Figure (7), an increase in the percentage of coarse fraction sand mixed with swelling soil from 0% to 80% reduced the swelling index (SI) of the three tested soils. For Soil (1), SI decreased from 0.0399 to 0.0091. For Soil (2), SI decreased from 0.0771 to 0.0183. For Soil (3), SI decreased from 0.0992 to 0.0201. Again, this observation is in line with what is observed with swelling potential and swelling pressure. Figure (10) shows the variation of the percentage of reduction in swelling index (R-SI) with the percentage, by weight, of coarse grained fraction soil (CF) available in the expansive soil. The best fit relationship is expressed as follows:

$$(R-SI) = 0.67 (CF) + 25 \quad (4)$$

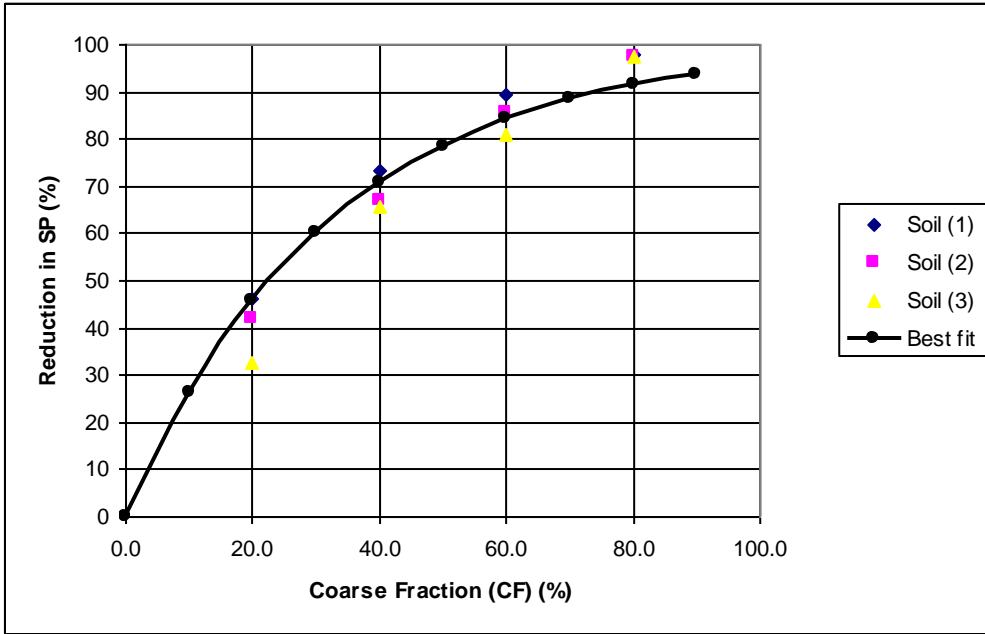


Fig. (8). Variation of the percentage of reduction in swelling potential with the percentage of coarse fraction sand added to the swelling soil

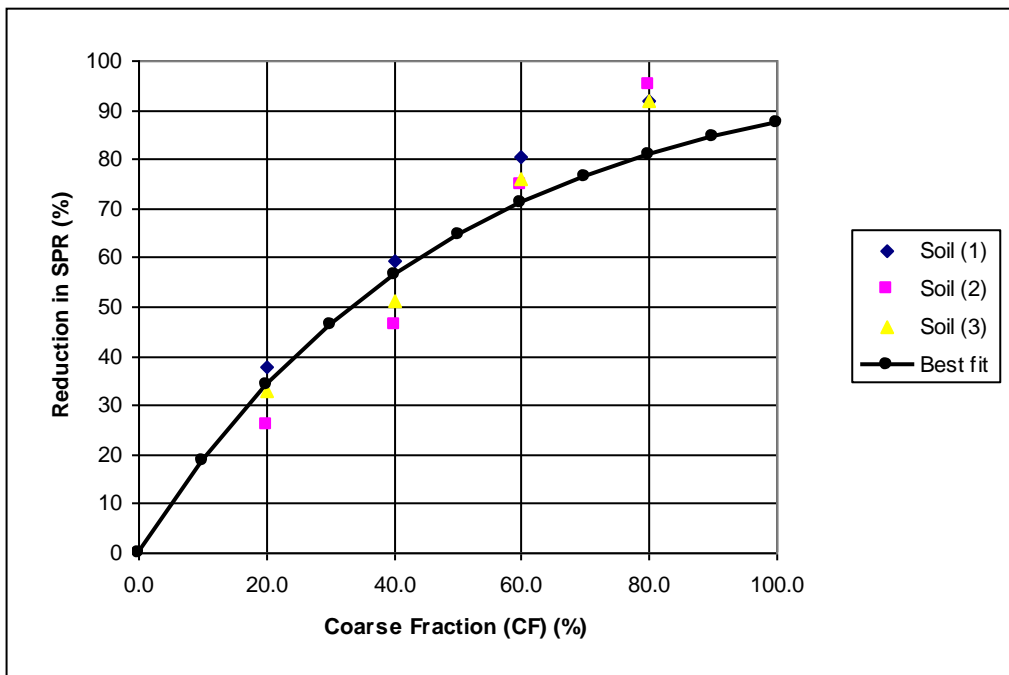


Fig (9). Variation of the percentage of reduction in swelling pressure with the percentage of coarse fraction sand added to the swelling soil.

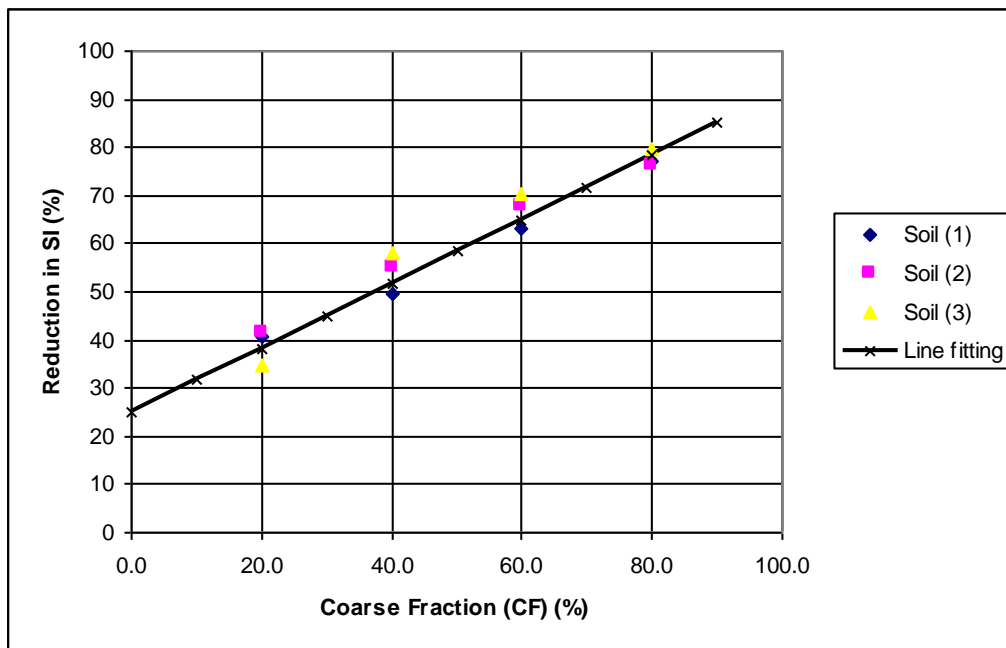


Fig. (10). Variation of the percentage of reduction in swelling index with the percentage of coarse fraction sand added to the swelling soil.

The three empirical relationships (2), (3), and (4) could be conveniently used to predict an estimated value for the expected reduction in SP, SPR, and SI of the expansive soil as a result of mixing a percentage of coarse fraction sandy soil (coarser than 0.425 mm). Naturally, these relationships are just preliminary and need more refinement in order to be widely accepted. However, increasing the number of tested swelling soil samples will improve and refine them. The results obtained in the current research are in agreement with the results published in the literature but using other treatment agents such as lime.

5. Conclusions

In the current paper, an experimental study is conducted in order to investigate the improvement in swelling characteristics of expansive soil due to the increase of its coarse fraction. The lab testing program used three sets of expansive soil from different sites and the tests were conducted according to ASTM "D4318". The expansive soils were mixed with sandy soil (coarser than 0.425 mm) with different percentages (20%, 40%, 60%, and 80%). For all tests the swelling characteristics; swelling potential, swelling pressure, and swelling index were recorded and analyzed. The study revealed that increasing the coarse fraction of swelling soil results in significant improvement of the swelling characteristics of expansive soil. Additionally, three preliminary correlations are introduced between the percentage of

coarse grained fraction of expansive soil and the expected percentage of reduction in swelling potential, swelling pressure and swelling index. Further lab testing data are needed in order to refine and improve these correlations. The technique of Neural Networks could present a significant tool for researchers to develop similar relationships, which might also include the influence of other physical and engineering properties of swelling soils. However, the literature shows that this technique requires larger number of data points in order to train the network effectively and consequently obtain more accurate and generalized relationships that could be used to predict the swelling behavior of soil.

6. References

- [1] AlMuhaidib, A., "Characteristics of Expansive Soil in the Kingdom of Saudi Arabia," *King Saud University Journal of Engineering Sciences*, 16 (2003), 1-34.
- [2] Dhowian, A. W., "Characteristics of Al-Ghatt Collapsing and Swelling Soils," *Proceedings of Symposium on Geotechnical Problems in Saudi Arabia*, Riyadh, Saudi Arabia, (1981), 3-32.
- [3] El-Sayed, S.T. "Soil of Swelling and Collapsing behavior, Mobaraz Town, Eastern Zone, Kingdom of Saudi Arabia." *Proceedings of Symposium on Geotechnical Problems in Saudi Arabia*, Riyadh, Saudi Arabia, (1981), 63-82.
- [4] Datye, K.R. "Linings and Stabilization of Slopes for Channels in Black Cotton Soil." *Proceedings of the 6th International Conference on Expansive Soils*, Delhi, (1987), 626-629.
- [5] Katti, R.K. and Katti, A.R. "Behavior of Saturated Expansive Soil and Control Methods." *A.A. Balkema, Rotterdam*, (1994), 853-861, 980-1004.
- [6] Byer, J.G. "Treatment of Expansive Clay Canal Lining." *Proceeding of the 4th International Conference on Expansive Soils*, Denver, USA, (1980).
- [7] Sorochan, E.A. "Construction of Buildings on Expansive Soil." *Proceeding of Geotechnika 5th*, France (1991), 272 – 295.
- [8] Marei et. al. "Improvement of Expansive Soil in Waterways Using Different Replacement Cushions." *Journal of the Egyptian Geotechnical Society*, 11 (2000), 1 – 10.
- [9] Satyanarayana, B. and Ranganatham, B.V. "A Rational Method of Predicting Swelling Potential, for Compacted Expansive Clays." *Proceeding of the 6th International Conference on SM and FE*, Canada, (1969), 92-96.
- [10] Komarnik, A. and David, D. "Prediction of Swelling Pressure of Clays." *ASCE Proceedings SM and FE Division*, 95 (1969), 209-225.
- [11] Mallikarjuna Rao. "A Proper Parameter for Correlation of Swell Potential and Swell Index for Remolded Expansive Clays." *M. Technical Dissertation Submitted to Dept. of Civil Eng. J.N.T. University college of Engineering, Kakinada, India*, (1988)
- [12] Mowafy, M.Y and G.E. Bauer. "Prediction of Swelling Pressure and Factors Affecting the Swell Behavior of Expansive Soils." *Transportation research record*, 1032 (1985), 23-28.

- [13] Erzin, Yusuf, and Orhan Erol. "Correlation for Quick Prediction of Swelling Pressure." *Electronic Journal of Geotechnical Engineering*, 9 (2004), 14-24.

تحسين خصائص التربة الانتفاشية عن طريق خلطها بالتربة الخشنة شريف محمد عبد الفتاح الخولى

قسم الهندسة المدنية، كلية الهندسة – جامعة القصيم، القصيم، المملكة العربية السعودية
فى إجازة عمل من معهد بحوث الإنشاءات، المركز القومى لبحوث المياه - مصر
(قدم للنشر فى 2 / 1 / 2008؛ وقبل للنشر فى 4 / 6 / 2008)

ملخص البحث. تنتشر التربة الانتفاشية فى مناطق كثيرة من العالم وخاصة فى المناطق الجافة وشبه الجافة ومنها المملكة العربية السعودية حيث تتواجد ترسيبات من هذه التربة ذات المشاكل عند أعماق مختلفة فى كثير من المناطق السكنية. عند البناء على هذه الطبقات يجب أخذ الكثير من الاحتياطات وذلك للتقليل من المخاطر المتوقعة على المنشآت. الباحثين والمهندسين إعتادوا على معالجة مشاكل هذه التربة بإحدى طريقتين إما باستبدال هذه الطبقات بكامل سمكها بتربة مناسبة أو عن طريق إضافة بعض المعالجات المختلفة التى تقلل من خواصها الانتفاشية وأثرها على المنشآت المقامة عليها.

الدراسة الحالية تطرح طريقة جديدة لمعالجة التربة الانتفاشية وتعديل خواصها الهندسية وذلك بخلطها مع تربة خشنة بنسب مختلفة لتحديد تأثير هذا الخلط على سلوك التربة الانتفاشية، وأجريت تجارب الانتفاش على الخلطات المجهزة وقياس معاملات الانتفاش (قابلية الانتفاش، جهد الانتفاش، معامل الانتفاش). أيضا تم تقديم بعض المعادلات الإحصائية البسيطة لترابط بين نسب خلط التربة الخشنة بالتربة الانتفاشية وبين معاملات الانتفاش المختلفة.

ELECTRONIC CONTROL OF SINGLE-PHASE INDUCTION MOTORS USING AC CHOPPER

M. A. Abdel-halim

A. F. Almarshoud

**Electrical Engineering Department, College of Engineering
Qassim University, Al-Qassim, Saudi Arabia**

masamie@hotmail.com

amarshoud@yahoo.com

(Received 15/7/2007; accepted for publication 20/11/2007)

Abstract

This paper suggests a versatile electronic method for efficient start, speed-control, direction-reversal, and plugging braking of single-phase induction motors. This is achieved by feeding the two-stator windings of a split-single-phase induction motor via two forced-commutated solid-state converters. AC chopping technique with possible edges control is applied. Thereby, high starting torques and low starting currents are realized. Reversing the direction of rotation and plugging braking are achieved by interchanging the sequence of voltages applied on the stator windings. Also, speed control is achieved at high motor efficiency as ac chopping results in less harmonic contents. The paper computes dynamic and steady-state performance characteristics of the motor using the suggested method. Then it compares them with other methods. For this purpose a state space mathematical model considering the discontinuities introduced by the electronic switches is developed to describe the system.

Key Words: single-phase induction motors, control of motors, solid-state control.

List of Symbols

H : machine and load inertia constant, sec.

i & u : p.u current and p.u voltage respectively

p : normalized time operator

R & X : p.u resistance and p.u reactance respectively

T : torque, p.u

α & β : firing angle and extinction angle respectively

ω_o & ω_r : base speed and p.u rotor speed respectively

Subscripts:

1 & 2 : stator- and rotor- side respectively
a & m : auxiliary- and main- winding respectively
d & q : direct- and quadrature- axis respectively
e & l : electrical and load respectively

1. Introduction

Single-phase induction motors of few watts up to about 5 hp are widely demanded. These motors are conventionally started by either phase splitting of the stator winding, using main and auxiliary windings together with capacitors connected to the auxiliary winding, or using commutator winding on the rotor to start it as a repulsion motor [1,2]. The speed is conventionally controlled using either winding tapings, variac, autotransformer, or series impedance [1-3]. The direction of rotation is usually reversed by interchanging the terminals of one of the stator windings [1].

Conventional methods for starting and speed control of single-phase induction motor need often quite expensive external electrical equipment. Moreover, they require mechanical switches, which are the most troublesome parts. These switches suffer from mechanical wear, which affects the motor performance. Electronic methods based on using a triac in series with the stator main winding [4-6] or using four triacs in a bridge topology [7] have been suggested to control the speed of the motor. Starting is still done by a capacitor in with the auxiliary winding. Other authors [8-10] have suggested and analyzed the performance of single-phase induction motors fed from inverter circuits. In this case either single-phase inverter is used with permanent capacitor motors, or two phase inverter is used when the capacitor is omitted. Both methods need complicated circuits with high cost. However, this seems to be acceptable solution when wide range of speed control is required.

One of the authors of the present paper has suggested in previous works [11-13] solid-state based methods to start, control the speed, and reverse the direction of rotation of the single-phase induction motors. One of these methods uses a naturally commutated electronic switch (triac) in each of the main and auxiliary winding. The motor is controlled by controlling the firing angle of the triacs. In the other methods forced commutated electronic switches (power transistors) are used in both the main and auxiliary windings. In this case the firing and extinction angles are controllable. Control of both the firing and extinction angles gives higher starting torque compared

with the resulting starting torque when the firing angle only is controlled. Although differ from method to another, large harmonic current contents are encountered leading to low motor running efficiency. Also, quite large harmonic contents are reflected on the supply side. Concerning the supply displacement angle, phase backing in natural commutation and forced commutation always give large lagging input current displacement angles, while extinction angle speed control in forced commutation can improve the displacement angle to the extent that it may go in the lead direction.

The present paper suggests a versatile control method suitable for all sizes of single-phase induction motors. Through this method the motor can be started even against high resistant torque. The speed may be efficiently controlled in a certain range. The method enables, also, reversing of the motor direction, and perform plugging braking.. The method uses a solid-state a.c chopper in each winding of a split-phase motor having two identical stator windings. The converter consists mainly of two power transistors integrated in two diode bridges. One in series with the supply, and the other is shunted with the winding to provide a freewheeling path. Power transistors are chosen to employ forced commutation. This enables chopping the applied voltage on each winding. Also edge cutting is possible when necessary. The use of freewheeling paths improves the utilization of the stored energy in the motor inductances. Thus, high starting torques at low supply current and enhanced running performance such as good power factor, low motor harmonic contents, and high motor efficiency are anticipated.

To determine the motor performance characteristics, a mathematical model has been developed. This model is based on using the dqo Kron's equivalent circuit for induction motor [14]. A computer program has been developed to simulate the system. With the aid of the program, the motor steady state and dynamic performance characteristics have been computed. The motor performance with the new method has been computed and compared with that obtained from other conventional and solid-state based methods.

2. Fundamentals of the Proposed Method

Figure (1) shows the circuit of a split phase induction motor having two identical main and auxiliary windings. Its windings are supplied from a single-phase source

through ac choppers. Each transistor has its own control circuit. But, the two transistors of any of the two windings are alternatively turned on and off. The applied voltage on the winding is equal to the supply voltage when the line transistor in series with it is on. When the freewheeling path is activated the applied voltage becomes zero. Figure (2) shows a general output voltage of the ac chopper. The motor draws its current from the supply once the line transistor is turned on. This supply current is forced to reduce to zero when the line transistor is turned off. Therein, the freewheeling transistor, which is turned on, carries the motor current.

To start the motor, the two line transistors are turned on and off once per half a cycle. The turning instants are chosen such that the stator currents have two time-shifted fundamental components. These components produce a component of rotating flux, which results in a starting torque. The direction of rotation of the motor is reversed easily by interchanging the firing and also the extinction angles of the two line transistors. At running condition, only the main winding is excited. The speed is controlled by chopping the voltage applied on it choosing the suitable duty cycle.

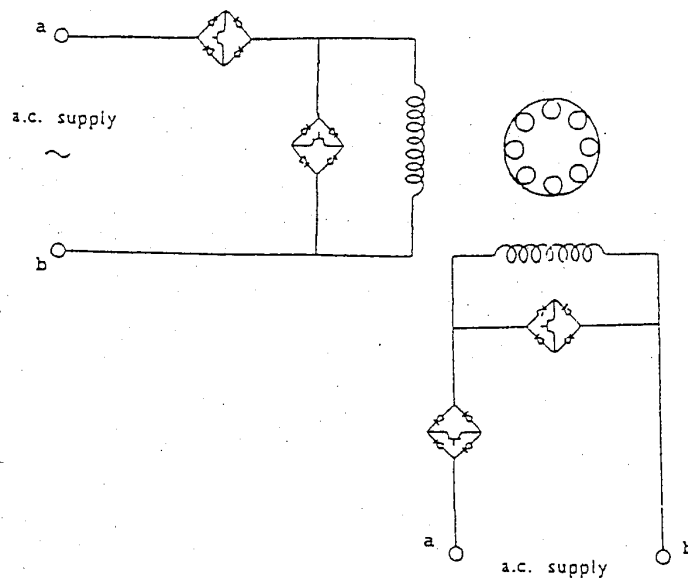


Fig. (1). Motor schematic diagram

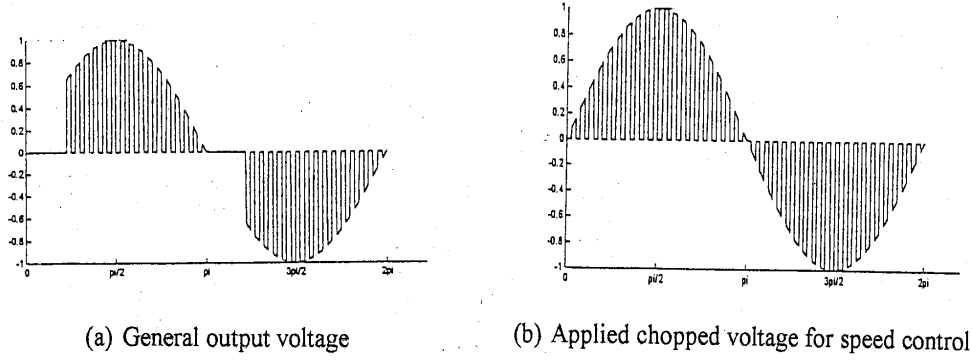


Fig. (2). AC chopper output voltage waveforms

3. Circuit and Mathematical Model

The induction motor is represented in the dqo reference frame by a four-coil attached to the stator member (Kron's model) [14]. The mathematical model will be derived assuming ideal electronic switches and neglecting the iron losses. Thus, the following matrix equation using p.u quantities is applied:

$$\begin{bmatrix} u_{1d} \\ u_{2d} \\ u_{2q} \\ u_{1q} \end{bmatrix} = \begin{bmatrix} R_{1d} + X_{11d}P & X_{12d}P & 0 & 0 \\ X_{12d}P & R_{2d} + X_{22d}P & X_{22q}\omega_r & X_{12q}\omega_r \\ -X_{12d}\omega_r & -X_{22d}\omega_r & R_{2q} + X_{22q}P & X_{12q}P \\ 0 & 0 & X_{12q}P & R_{1q} + X_{11q}P \end{bmatrix} \begin{bmatrix} i_{1d} \\ i_{2d} \\ i_{2q} \\ i_{1q} \end{bmatrix} \quad \dots(1)$$

u_{1d} and u_{1q} are set equal to the supply voltage when the associated line transistor is activated, and set equal to zero when the associated free-wheeling path is activated. Since the rotor is a squirrel cage type, the two voltages of the rotor in the direct- and quadrature- axis are zeros. To start the motor, the ac chopper circuits are controlled to give the waveforms of u_{1d} and u_{1q} shown in figure (3). Thus

$$\begin{aligned} u_{1d} &= \sin\omega t & \alpha_m \leq \omega t \leq \beta_m, \quad \pi + \alpha_m \leq \omega t \leq \pi + \beta_m \\ &= 0 & \text{elsewhere} \\ u_{1q} &= \sin\omega t & \alpha_a \leq \omega t \leq \beta_a, \quad \pi + \alpha_a \leq \omega t \leq \pi + \beta_a \\ &= 0 & \text{elsewhere} \end{aligned}$$

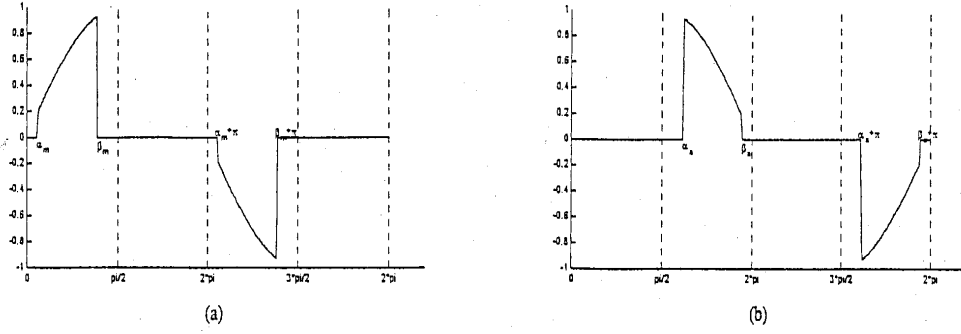


Fig. (3). Applied voltage for starting

(a) Main winding voltage

(b) Auxiliary winding voltage

At running conditions, one of the stator windings is excited while the other winding is disconnected from the supply. Speed control is achieved by chopping the voltage applied to the winding. This voltage is shown in figure (2-b). u_{1d} can be expressed as [15]

$$u_{1d} = 0 \quad J 2\pi/P \leq \omega t \leq J 2\pi/P + \alpha$$

$$u_{1d} = \sin \omega t \quad J 2\pi/P + \alpha \leq \omega t \leq (J + 1) 2\pi/P$$

Where P = frequency ratio (chopping frequency/supply frequency)

$$J = 0, 1, 2, \dots, P/2$$

The output voltage is controlled by the duty cycle (K), which is expressed as follows:

$$K = (2\pi/P - \alpha)/(2\pi/P)$$

Rewriting Eqn. 1 in a split form yields:

$$[u] = [R][i] + [X]p[i] + \omega_r [G][i] \quad (2)$$

$$\text{Where: } [i] = [i_{1d}, i_{2d}, i_{1q}, i_{1q}]^T,$$

$$[u] = [u_{1d}, 0, 0, u_{1q}]^T,$$

$[R]$ is the resistance matrix, $[X]$ is the reactance matrix, and $[G]$ is the rotational voltage coefficient matrix. Rearranging the equation terms, the following state space form is obtained:

$$p[i] = [A][i] + [B][u] \quad (3)$$

$$\text{Where: } [A] = -[X]^{-1} ([R] + \omega_r [G]), \text{ and } [B] = [X]^{-1}$$

The equation for the rotor speed is:

$$p \omega_r = 1/(2H\omega_o) [T_e - T_1] \quad (4)$$

The electrical torque, in p.u., is given by [14]:

$$T_e = 2[X_{12q} i_{1q} i_{2d} + X_{22q} i_{2q} i_{2d} - X_{12d} i_{1d} i_{2q} - X_{22d} i_{2d} i_{2q}] \quad (5)$$

The supply current is given by

$$i_s = F_d i_{1d} + F_q i_{1q} \quad (6)$$

where F_d and F_q are switching functions take either 1 or 0 value. The value is 1 if the associated line transistor is on, otherwise it is 0.

4. Digital Simulation

A computer program has been developed to determine the performance of the motor. The state-space matrix equation is solved by numerical integration using the fourth-order Rung-Kutta technique [16] with the appropriate initial conditions. During any transient condition, the state space variables are the motor four currents in addition to the rotor speed. These variables are governed by Eqns. 3 & 4. At steady-state conditions the speed pulsation is neglected, and thus the speed is considered constant. Consequently, the motor currents are the only state variables, and they are governed by Eqn. 3. The steady-state currents are reached after few cycles to allow the transient currents to die down. Once the current waveform and instantaneous torques are obtained, conventional numerical techniques [16], employing integration trapezoid rule and Fourier series analysis, are applied to compute the motor performance indices [16, 17] such as the current effective values, the fundamental current components, the displacement angle, the total harmonic distortion, the power factor, the average developed torque and the motor efficiency .

5. Results and Discussions

A single-phase induction motor of identical main and auxiliary windings has been chosen to apply the proposed method. The specifications of the motor are given in Table 1. The load is assumed to reflect a torque which is proportional to the speed. The motor full-load torque is about 0.4 p.u. The motor and load data have been fed into the program and transient and steady state performance characteristics have been computed.

The effect of variation of turn-on angle of the line transistors for a constant conduction angle of 90° upon the motor average starting-torque is displayed in figure (4). The figure shows that when the turn-on angle of the main transistor is smaller than that of the auxiliary one the average starting torque is positive. When the main-winding transistor turn-on angle exceeds that of the auxiliary one, the average torque

reverses its direction. It is clear from the computed results that the starting torque produced by the motor employing the suggested method reaches a value higher than twice the full load torque. Therefore, this method is suitable for starting the motor with loads that reflect high resistive torque at starting. The starting current variation with the transistor turn-on angle is shown in figure (5). The supply starting current is about 2.8 p.u at the condition that gives maximum starting torque ($\alpha_m = 0^\circ$ and $\alpha_a = 65^\circ$) which is good.

Figure (6) shows the speed transient of the motor when started at main and auxiliary turn-on angles of 0° and 90° and turn-off angles of 90° and 180° respectively, then plugging braking is employed by interchanging the order of both the turn-on and turn-off angles.

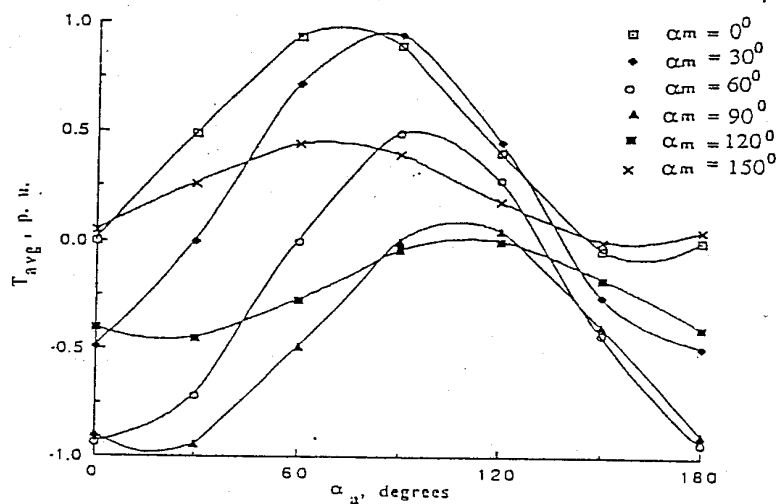


Fig. (4). Motor starting torque

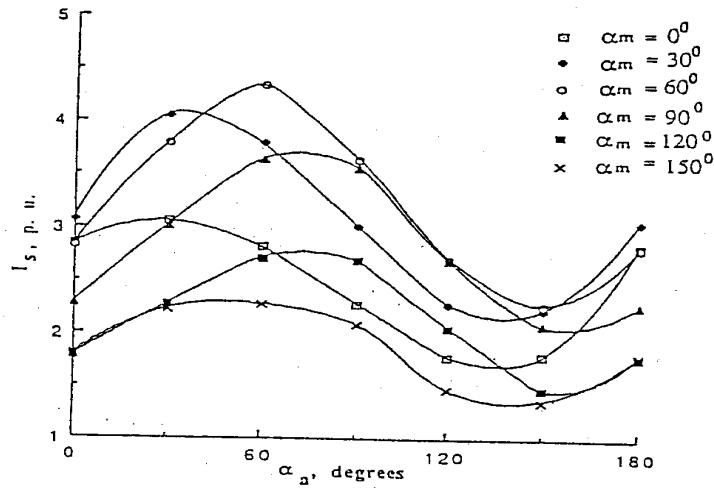


Fig. (5). Supply starting current

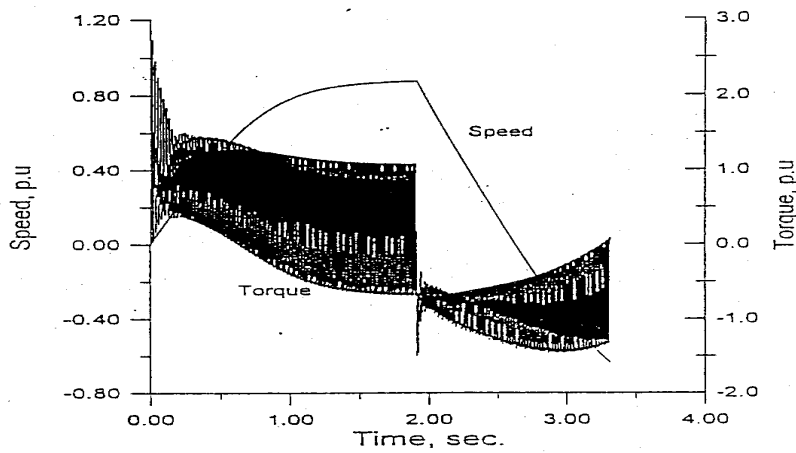


Fig. (6). Starting followed by plugging braking

The steady state performance characteristics of the loaded motor have been computed for two different chopping frequency ratios; 10 and 20. The duty cycle has been varied to control the speed. Like all other methods utilizing ac voltage controller, the achieved speed control range is smooth but not wide. The motor and supply current variations with the speed are depicted in figures (7) and (8). They have been compared with those obtained using variac [11], triac [11], forced-commutation employing firing angle control [12] and forced commutation with free wheeling paths employing also firing angle control [13]. The results reveal that the currents when using the ac chopper based method are less compared with other methods. They approach the variac method currents. Figure (9) compares the current displacement

angle using the ac chopper with those obtained when using the other methods [11-13]. It is clear that using ac chopper keeps the displacement angle very close to the natural impedance angle of the motor as the case of variac control. The motor harmonic contents are less in case of using the ac chopper compared with all other methods employing electronic switches. Its value decreases as the frequency ratio increases (figure 10). Although ac chopping decreases the harmonic contents in the motor current, it reflects more harmonic contents upon the supply side (figure 11). But, it should be noted that these harmonics are of high frequencies (almost integer multiples of the chopping frequency). Consequently, they can be easily filtered. The supply power factor is midway between the natural commutation method and the forced commutation methods (figure 12). The motor efficiency is improved when the speed is controlled using the ac chopper (figure 13). This is due to the less harmonic contents in the motor currents.

Computed voltage and current waveforms for frequency ratio equals 10 and duty cycle equals 0.7 are shown in figure (14).

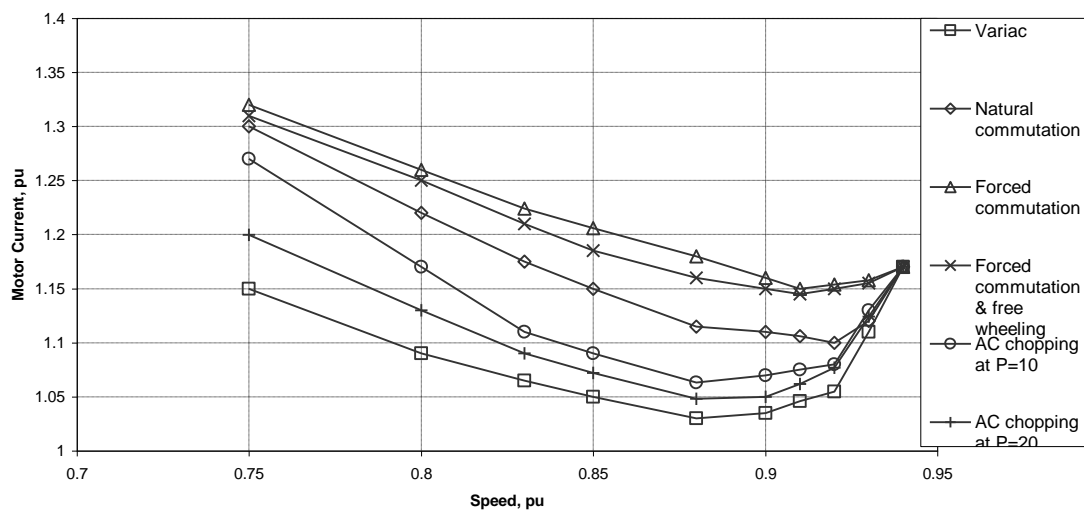


Fig. (7). Motor current variation with the speed

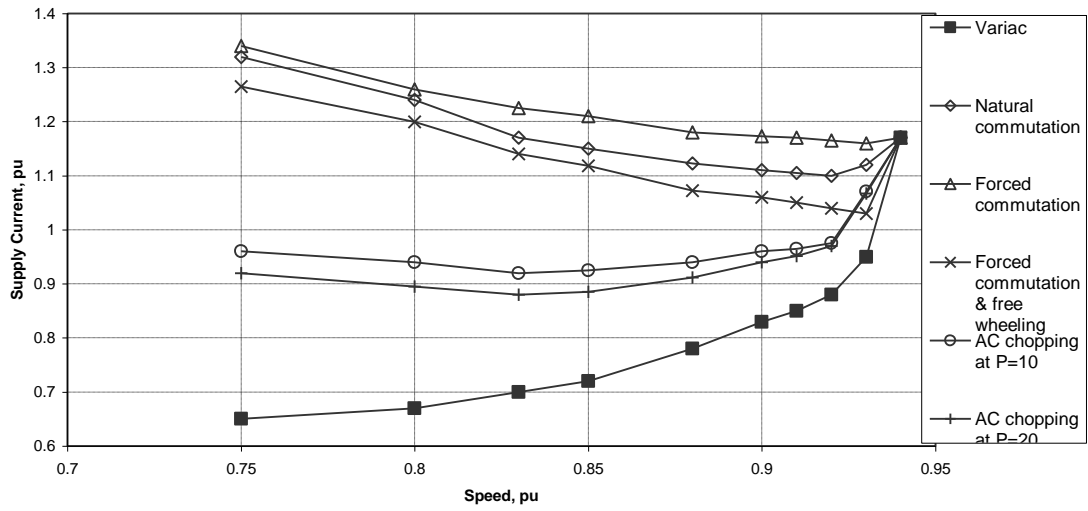


Fig. (8). Supply current variation with the speed

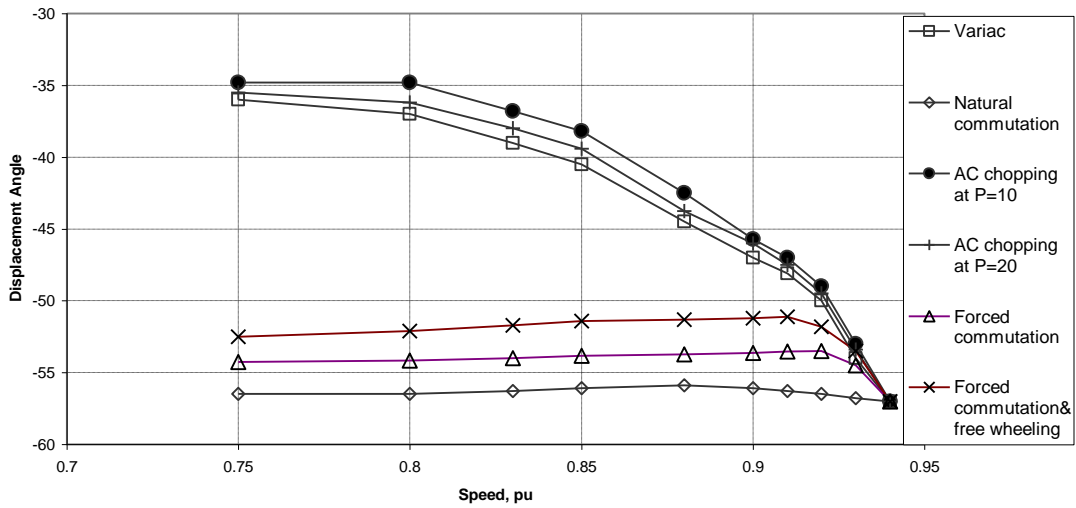


Fig. (9). Displacement angle variation with the speed

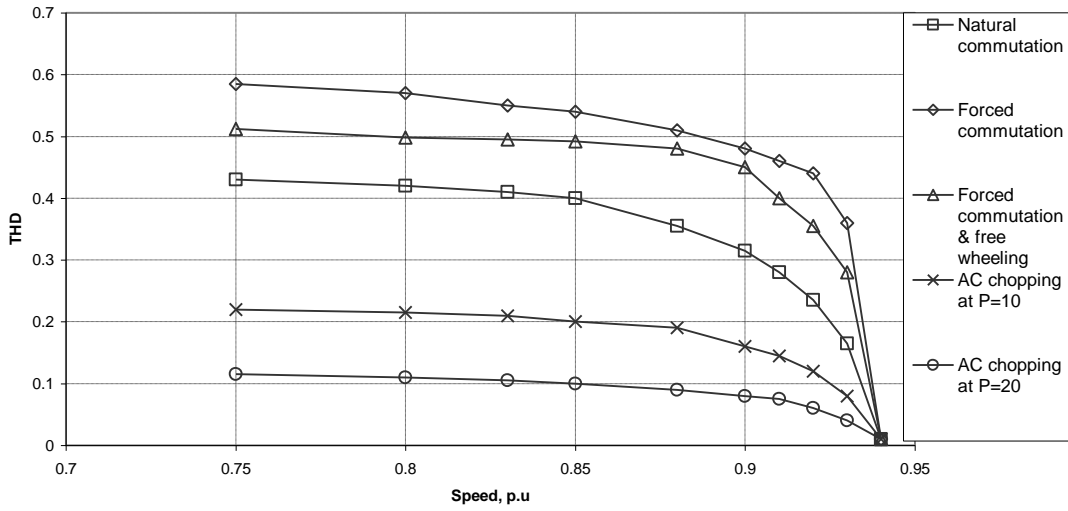


Fig. (10). Total harmonic distortion factor of the motor current

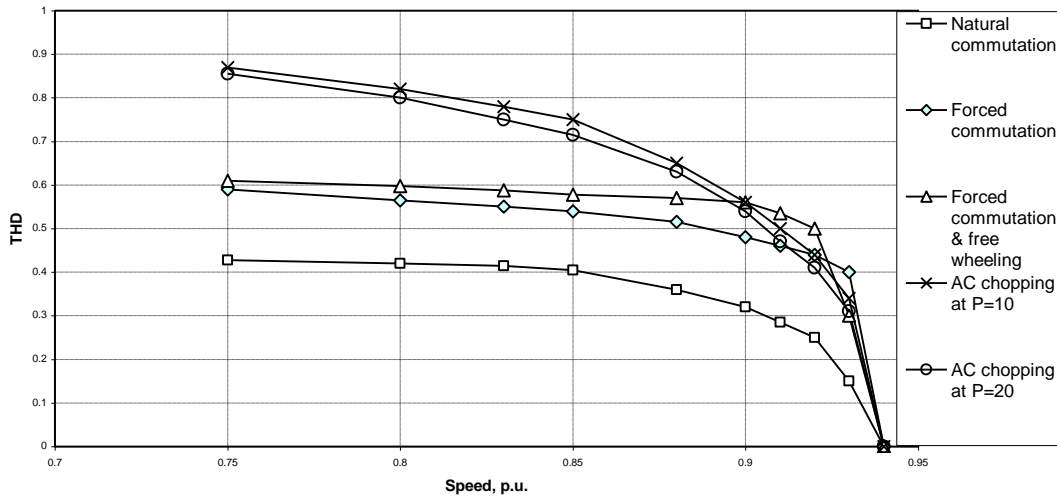


Fig. (11). Total harmonic distortion factor of the supply current

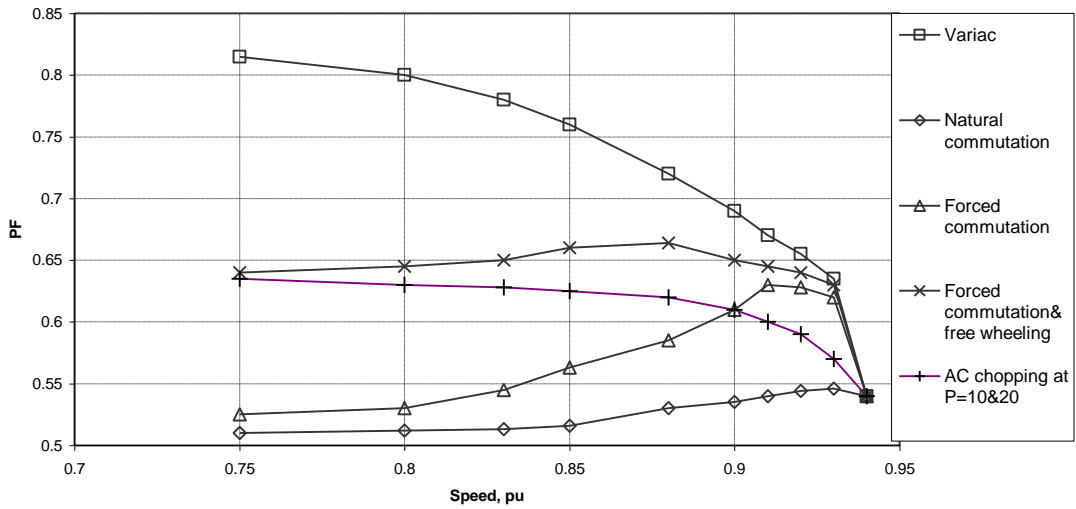


Fig. (12). Supply power factor

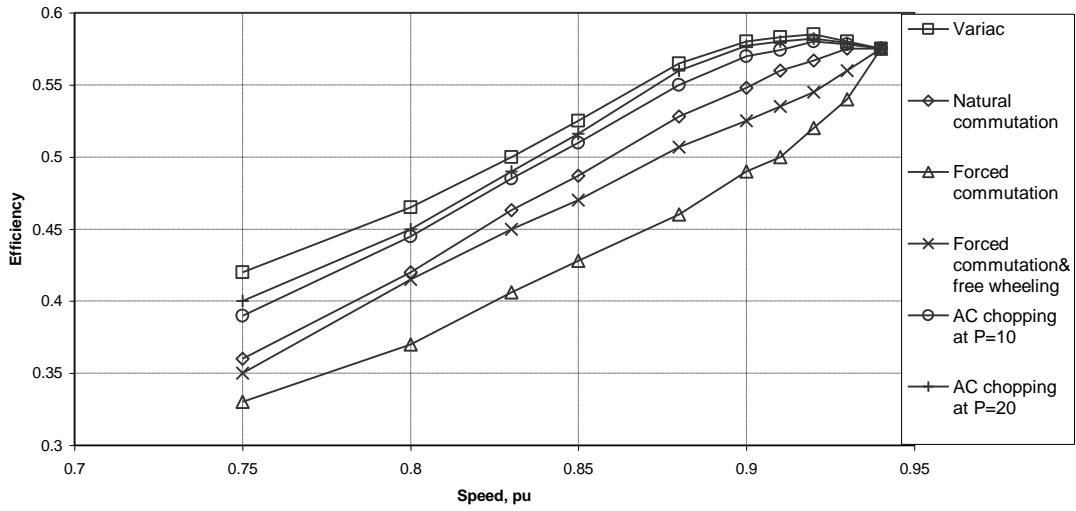


Fig. (13). Motor efficiency

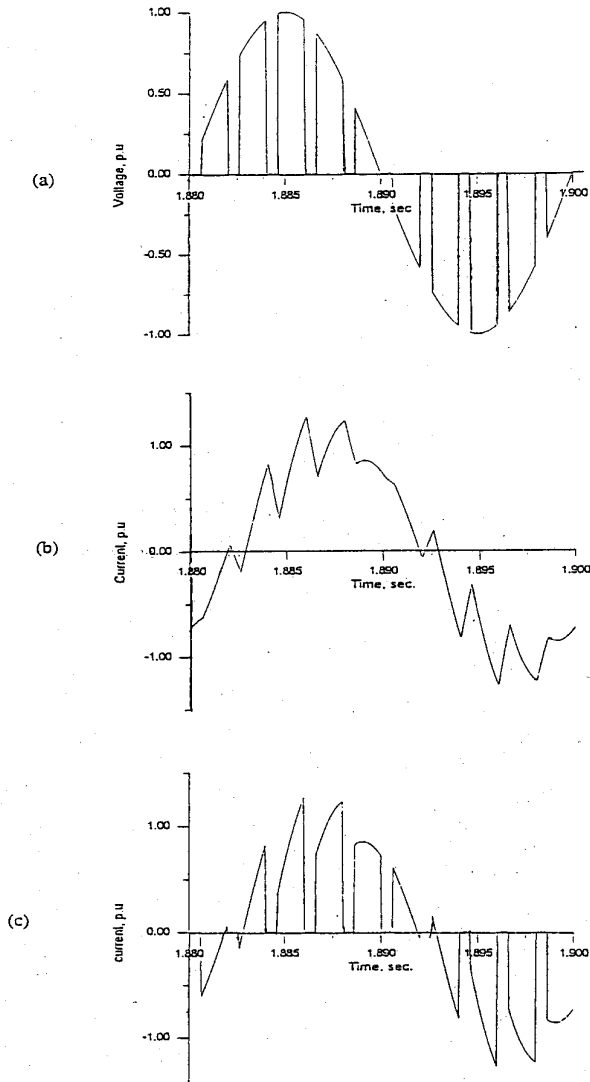


Fig. (14). Computed voltage and current wave-forms at a frequency ratio of 10 and duty cycle equals 0.7.

a) Voltage b) Motor current c) Supply current

6. Conclusions and Recommendations

The suggested versatile electronic method has proved its validity and advantage for controlling single-phase induction motors. By this method the motors could be started, speed-controlled, reversed and braked. The computed performance characteristics of a single-phase motor driven by the proposed converter reveal that high starting torque is achieved at low starting current. The direction of rotation could be reversed and plugging braking is possible. High frequency chopping results in low motor current harmonic contents, and consequently less copper losses and good efficiency. The ac chopper does not adversely affect the displacement angle of the current, as does the natural commutation method. The harmonic currents reflected on the network are relatively large compared with the other methods especially the natural commutation method. Nevertheless, they can be easily filtered as they are of higher orders.

It is recommended to include the iron and switching losses in future works for accurate evaluation of the motor efficiency.

7. References

- [1] Chapman, S. J., *Electric Machinery Fundamentals*, 4th edition, New York, McGraw-Hill, 2005.
- [2] Veinott, C. G. and Martin J. E., *Fractional and Subfractional Horsepower Electrical Motors*, New York: McGraw-Hill, 1986.
- [3] Veinott, C. G., "Performance Calculation on L- and T-Connected Tapped-Winding Capacitor Motors," *IEEE Trans. on Power Apparatus and Systems*, Vol. PAS-96, No. 4, (July/August 1977) , pp 1137-1144.
- [4] Cattermole, D. E., Davis, R. M. and Wallace, A. K., "The Design Optimization of a Split-Phase Fan Motor with Triac Voltage (Speed) Control," *IEEE Trans. on Power Apparatus and Systems*, Vol. PAS-94, No. 3, (May/June 1975), pp. 778-785.
- [5] Cattermole, D. E. and Davis, R. M., "A Triac Voltage (Speed) Control for Improved Performance of Split-Phase Fan Motors," *IEEE Trans. on Power Apparatus and Systems*, Vol. PAS-94, No. 3, (May/June 1975), pp. 786-791.

- [6] Fatih, N., "Performance Characteristics of a Triac-Controlled Single-Phase Induction Motor Having Space Harmonics in its Magnetic Field," *Electric Power Systems Research*, Vol. 14, (1988), pp. 97-102.
- [7] Julian, A. L., Wallace, R. S. and Sood, P. K., "Multi-Speed Control of Single-Phase Induction Motors for Blower Applications," *IEEE Transactions on Power Electronics*, Vol. 10, No. 1, (1995), pp.72-77.
- [8] Homat, M., and Lipo, T. A., "Adjustable-Speed Drive with Single-Phase Induction Machine for HVAC Applications," *Proc. of IEEE 32nd Annual Power Electronics Specialist Conference*, (2001), pp. 1446-1451.
- [9] Blaabjerg, F., Lungeanu, F., Skaug, K. and Aupke, A., "Comparison of Variable Speed Drives for Single-Phase Induction Motors," *Proc. of the Power Conversion Conference*, Vol. 3, (2002), pp. 1328-1333.
- [10] Zadeh, S. V. and Reicy, S. H., "Sensorless Vector Control of Single-Phase Induction Motor Drives," *Proc. of the Eighth International Conference on Electrical Machines and Systems*, Vol. 3, (2005), pp. 1838-1842.
- [11] Abdel-halim, M. A., "Solid State Control of Single Phase Induction Motor," *Electrical Machines and Power System Journal*, Vol. 24, No. 6, (1996), pp. 623-638.
- [12] Abdel-halim, M. A., "Control of Single Phase Induction Motor Using Forced-commutated Electronic Switches," *Electrical Machines and Power System Journal*, Vol. 25, No. 6, (1997), pp. 1119-1134.
- [13] Abdel-halim, M. A., "Control of Single Phase Induction Motor Using Forced-Commutated Electronic Switches and Freewheeling Paths," *Electrical Machines and Power System Journal*, Vol. 27, No. 11, (1999), pp. 1201-1213.
- [14] Adkins, B. and Harley, R. G., *The General Theory of Alternating Current Machines*, London: Chapman and Hall, 1975.
- [15] Mohamadin, A. L. and Addoweesh, K. E. "Evaluation of the Performance of Chopper Type AC Voltage Controller," *International Journal of Electronics*, Vol. 67, No. 4, (1989), pp. 669-683.
- [16] Akai, T. J. *Applied Numerical Methods for Engineers*, New York: John Wiley & Sons, 1993.
- [17] Rashid, M. H., *Power Electronics; Circuits, Devices and Applications*, 3rd Edition, London: Prentice Hall, 2004.

Table 1: Motor Specifications

Voltage	220 V	Current	5.62
Hp	2/3	No. of poles	4
Frequency	50 Hz	Speed	1420 rpm
R_{1d}, R_{1q}	4.23 ohm	R_{2d}, R_{2q}	6.24 ohm
X_{12d}, X_{12q}	59.9 ohm	$X_{11d}, X_{11q}, X_{22d}, X_{22q}$	64.3 ohm

التحكم الإلكتروني في محركات الحث أحادية الطور باستخدام مقطع التيار المتردد

محمد عبد السميع عبد الحليم
عبد الرحمن بن فهد المرشود
قسم الهندسة الكهربائية- كلية الهندسة- جامعة القصيم
القصيم- المملكة العربية السعودية
(قدم للنشر في 2007/7/15؛ وقبل للنشر في 2007/11/20)

ملخص البحث. يقترح البحث طريقة الكترونية موحدة لبدء الحركة والتحكم في السرعة وعكس اتجاه الدوران وفرملة محركات الحث أحادية الطور، وتعتمد هذه الطريقة على تغذية ملفي العضو الثابت من خلال مغيرين الكترونيين يستخدمان مبدأ الإخماد القسري لتبديل التيار، ويتم التحكم في المحرك بتشغيل المغير كمقطع للتيار المتردد مع التحكم في حواف الجهد، ومن ثم يمكن الوصول إلى عزم عال لبدء الحركة مع تيار بدء منخفض، أما عكس اتجاه الحركة وفرملة المحرك فتتطلب بتغيير تتابع الجهد المطبق على ملفات العضو الساكن، كما يتم التحكم في السرعة بتغيير دورة واجب مقطع التيار المتردد. التحكم في السرعة باستخدام هذه الطريقة يضمن كفاءة عالية للمحرك حيث أن التوافقيات قليلة.

يقدم البحث حسابات كاملة لخواص أداء المحرك في كل من حالتي الأداء المستقر والأداء الديناميكي، ويقارن تلك الخواص بتلك المرتبطة بطرق الكترونية أخرى. وتعتمد حسابات خواص الأداء على نموذج فضاء حالة. هذا النموذج يستخدم التيارات كمتغيرات، ويأخذ في الاعتبار حالات عدم الاتصال في التيار المرتبطة بوجود المفاتيح الإلكترونية.

Voltage and Frequency Control of Self-Excited Short-Shunt Induction Generator

H. H. Hanafy A. M. Gesraha M. M. Abd-Elaziz A. F. Zobaa
Electrical power and Machines Department, Faculty of Engineering
Cairo University, Giza, Egypt
E-mails??????

(Received 18/10/2007; accepted for publication 24/3/2008)

Abstract

This paper discusses the steady-state analysis of Self Excited Short-Shunt Induction Generator (SESSIG) driven by unregulated turbine. A new analytical technique has been explained to choose the appropriate set values of both shunt and series capacitances to control the magnitude and frequency of the load voltage. The study shows that there are speed ranges over which both the load voltage and frequency could be maintained constant, by varying the excitation capacitances, according to the load conditions. The speed range and the required capacitances are calculated for different load conditions. The self excitation at no-load conditions and a new technique to calculate the required excitation capacitance are also discussed.

Key words: Induction generator, self-excitation, voltage and frequency control.

1. Introduction

A capacitor self-excited induction generator offers certain advantages over a conventional synchronous generator as a source of isolated power supply. These advantages include reduced unit cost, brush-less rotor (squirrel cage construction), absence of a separate DC source, low maintenance, and the ability of generating power at variable speeds. Capacitor self-excitation of induction machine is now known phenomenon and has been researched in depth [1-5].

The major problem in the operation of the stand-alone induction generator is that of guaranteeing the self-excitation. Self-excitation of induction generator and its sustenance depend on the appropriate combination of speed, load, and terminal capacitance in relation to the magnetic non-linearity of the machine. If the terminal voltage and frequency are known, as in the case of a machine connected to an infinite bus bar, the prediction of performance is straightforward. However in a capacitor – excited generator used as an isolated power source, both the terminal voltage and

frequency are unknown and have to be computed for a given speed, excitation capacitance, and load impedance [3].

The terminal capacitance on such machines must have a minimum value so that self-excitation is possible. Usually numerical methods are used to estimate this value. Grantham et. al.[6] and Tandon et. al. [7] studied the onset of self excitation and minimum capacitance requirements based on the characteristic polynomial obtained from transient representation of the machine. This method requires sets of results obtained from the numerical solution to the characteristic polynomial satisfying certain criteria before inferring the minimum capacitance at which self-excitation occurs for a particular speed and load. Malik and Mazi [8] suggested an indirect procedure, based on the steady state equivalent circuit model, to test the self-excitation of an induction generator. The indirect methods involve solutions requiring some initial guess in a trial and error procedure. Al-Jabre and Alolah [9] and Chan [10-12] presented direct methods to test the self-excitation of an induction generator and compute the minimum capacitance for self-excitation.

Rigorous research on the SEIG has been handled by many researchers [13-16], most of the published work focused on studying the effect of varying the load connected across the machine terminals for a given capacitance and speed, i.e. attention is mainly focused on the constant-speed mode of operation, which is not surprising, as the SEIG is usually driven by a turbine which has a variable speed, such as wind and hydro turbines. The difficulty of controlling the voltage and frequency of the SEIG under varying the speed has found in limiting usage of unregulated prime mover. However, the recent advancements in power electronics have made it possible to regulate the SEIG in many different ways.

This paper introduces a new simple and direct method of finding the minimum capacitance required for self-excitation, also a new analytical technique to analyze the steady-state behavior of the SESSIG with unregulated prime mover (such as wind turbine) will be presented. A new strategy will be presented in this paper to maintain both the terminal voltage and frequency of a SESSIG constant at rated values under different operating conditions (variable speed, load impedance and power factor) by selecting the most appropriate pair of capacitances.

2. Mathematical Model of Three-Phase Induction Generator

2.1 Steady-state equivalent circuit

The steady-state equivalent circuit per phase of a SESSIG is shown in figure (1). The generator core losses have been ignored. All the circuit parameters, except magnetizing reactance, are assumed to be constant and unaffected by saturation.

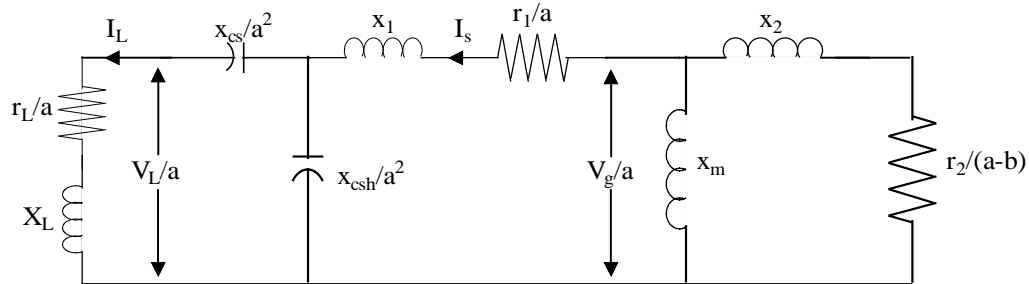


Fig. (1). The steady-state equivalent circuit per phase of a SESSIG.

Where:

- r_1 P.U. resistance of stator per phase;
- r_2 P.U. resistance of rotor per phase;
- x_1 P.U. reactance of stator per phase (at nominal frequency);
- x_2 P.U. reactance of rotor per phase (at nominal frequency);
- x_m P.U. magnetizing reactance per phase (at nominal frequency);
- a P.U. frequency;
- b P.U. speed;
- x_{csh} P.U. reactance of shunt capacitor (at nominal frequency);
- x_{cs} P.U. reactance of series capacitor (at nominal frequency).
- r_L P.U. resistance of the load per phase;
- x_L P.U. reactance of the load per phase (at nominal frequency);

2.2 No-load conditions

Figure (2) shows the equivalent circuit per phase at no-load conditions, the loop equation for the current I_s can be written as

$$I_s Z = 0 \quad (1)$$

where Z is the net loop impedance given by

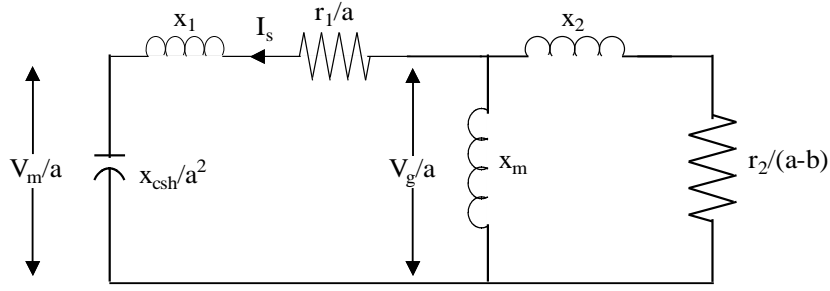


Fig. (2). The steady-state equivalent circuit per phase of a SESSIG at no-load conditions.

$$Z = Z_1 + \frac{Z_2 Z_m}{Z_2 + Z_m} \quad (2)$$

Where

$$Z_1 = R_1 + j(x_1 - X_{sh})$$

$$Z_2 = R_2 + jx_2$$

$$Z_m = jX_m$$

and

$$R_1 = \frac{r_1}{a}, \quad R_2 = \frac{r_2}{a-b}, \quad X_{sh} = \frac{x_{csh}}{a^2}$$

From (1) since under steady-state

$$I_s \neq 0$$

Therefore,

$$Z = 0$$

which implies that both real and imaginary parts of the right-hand side of Eqn. 2 would be separately zero. This equation could be simplified to the following two nonlinear equations:

The real part yields

$$D_1 x_m^2 + D_2 x_m + D_3 = 0 \quad (3)$$

where

$$D_1 = R_1 + R_2$$

$$D_2 = 2R_1 x_2$$

$$D_3 = R_1 (R_2^2 + x_2^2)$$

and the imaginary part yields

$$x_{csh} = \left\{ x_1 + \frac{R_2^2 x_m + x_2 x_m X_{2m}}{R_2^2 + X_{2m}^2} \right\} * a^2 \quad (4)$$

where

$$X_{2m} = x_2 + x_m$$

From the magnetization characteristic of the machine (figure 3), the saturation portion of this characteristic can be linearized and expressed mathematically in the form [3]:

$$\frac{V_g}{a} = K_1 - K_2 x_m \quad (5)$$

From the equivalent circuit shown in figure (2), the terminal voltage at no-load (V_m) could be written in terms of the generated voltage (V_g) as follows:

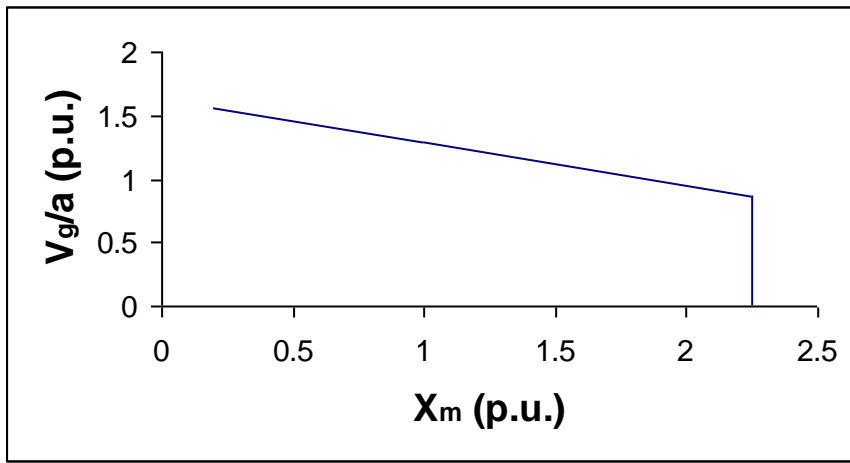


Fig. (3). The magnetization characteristic of the machine.

$$|V_m| = \frac{V_g X_{sh}}{\sqrt{R_1^2 + (x_1 - X_{sh})^2}} \quad (6)$$

Based on the analytical technique explained above, the required set values of the p.u. speed “ b ” and the excitation capacitor “ x_{csh} ”, to achieve self excitation with specified values of no-load terminal voltage “ V_m ” and frequency “ a ”, could be computed using the following algorithm:

- 1) Assume a value of “ b ” ($b > a$).
- 2) For the specified values of “ a ” and “ b ” get “ x_m ” from Eqn. 3.
- 3) Get “ x_{csh} ” from Eqn. 4.
- 4) Get “ V_g ” from Eqn. 5.
- 5) Get “ $|V_m|$ ” from Eqn. 6.
- 6) If “ $|V_m|$ ” equals the desired value stop. Else go to step (1) and change the assumed value of “ b ”.

From the above algorithm one can notice that there is only one restriction on the required value of the p.u. speed “ b ”, which is the value of the p.u. speed must be greater than the p.u. value of the frequency.

2.3 On-load conditions

In this section, a direct simple method to predict the required values of shunt and series capacitances for general inductive-load conditions is developed to achieve the desired values of load voltage and frequency.

Referring to the equivalent circuit of SESSIG shown in figure (1), the loop equation for the current I_s can be written as

$$I_s Z = 0 \quad (7)$$

Since under steady-state excitation

$$I_s \neq 0.$$

Therefore,

$$Z = 0$$

where

$$Z = Z_1 + Z_2 + Z_3 \quad (8)$$

$$Z_1 = R_1 + jX_1$$

$$Z_2 = \frac{jX_m(R_2 + jX_2)}{R_2 + jX_{2m}}$$

$$Z_3 = \frac{-jX_{sh}(R_l + j(x_L - X_s))}{R_l + j(x_l - X_c)}$$

$$X_s = \frac{X_{cs}}{a^2}, \quad R_L = \frac{r_L}{a}, \quad X_c = X_s + X_{sh}$$

Equation 8 after separation into real and imaginary parts could be rearranged into the following two equations which are functions of X_{sh} and X_s , denoted as $f(X_{sh}, X_s)$ and $g(X_{sh}, X_s)$

$$f(X_{sh}, X_s) = A_1 + A_2 X_{sh} + A_3 X_s + A_4 X_{sh} X_s = 0 \quad (9)$$

$$g(X_{sh}, X_s) = B_1 + B_2 X_{sh} + B_3 X_s = 0 \quad (10)$$

where

$$A_1 = R_L \left(R_1 + \frac{R_2 x_m^2}{R_2^2 + X_{2m}^2} \right) - x_L \left(x_1 + \frac{R_2^2 x_m + x_2 x_m X_{2m}}{R_2^2 + X_{2m}^2} \right)$$

$$A_2 = x_1 + x_L + \frac{R_2^2 x_m + x_2 x_m X_{2m}}{R_2^2 + X_{2m}^2}$$

$$A_3 = x_1 + \frac{R_2^2 x_m + x_2 x_m X_{2m}}{R_2^2 + X_{2m}^2}$$

$$A_4 = -1$$

$$B_1 = \left(R_1 + \frac{R_2 x_m^2}{R_2^2 + X_{2m}^2} \right) x_L + \left(x_1 + \frac{R_2^2 x_m + x_2 x_m X_{2m}}{R_2^2 + X_{2m}^2} \right) R_L$$

$$B_2 = - \left(R_1 + R_L + \frac{R_2 x_m^2}{R_2^2 + X_{2m}^2} \right)$$

$$B_3 = \frac{-R_2 x_m^2}{R_2^2 + X_{2m}^2} - R_1$$

The load voltage could be given by

$$|V_L| = \frac{V_g X_{sh} \sqrt{R_L^2 + x_L^2}}{\sqrt{(R_1 + E_1)^2 + (x_1 + E_2)^2} \sqrt{R_L^2 + (x_L - X_c)^2}} \quad (11)$$

where

$$E_1 = \frac{R_L X_{sh}^2}{R_L^2 + (x_L - X_c)^2}$$

$$E_2 = \frac{-X_{sh} \{ R_L^2 - (x_L - X_s)(x_L - X_c) \}}{R_L^2 + (x_L - X_c)^2}$$

Based on the analytical technique explained above, the required set values of “ x_{csh} ” and “ x_{cs} ”, to achieve the specified values of the load terminal voltage “ V_L ” and the operating frequency “ a ”, at the operating speed “ b ” and load impedance (r_L, x_L) could be computed using the following algorithm.

- 1) Assume V_g ;
- 2) Get x_m from Eqn. 5;
- 3) Solving Eqns. (9),(10) to get “ X_{sh} ” and “ X_s ” then get “ x_{csh} ” and “ x_{cs} ”;
- 4) Calculate $|V_L|$ from Eqn. 11;
- 5) If $|V_L|$ equals the desired value stop. Else go to step (1) and change the assumed value of “ V_g ”.

3. Simulation Results

The performance characteristics of a capacitor excited, 3.7 KW, squirrel cage induction generator [13, 14] (detailed data is given in Appendix A) are calculated via the proposed technique, the computed results for the given machine are presented in the following sections.

3.1 No-load conditions

Figure (4) shows the no-load terminal voltage of the machine and the needed capacitance for self excitation versus the p.u. value of the operating speed at constant frequency ($a=1.0$ p.u.), one can notice that the terminal voltage increases and the needed excitation capacitance decreases with the increasing of the speed and the rise of terminal voltage is limited by the saturation of the magnetic circuit of the machine. These results have good agreements with that obtained in [13, 14]

Figure (5) shows the variation of the needed capacitance and frequency versus the p.u. value of the speed to maintain the terminal voltage under no load constant at the rated value ($V_m=1.0$ p.u.). It may be noted that, as the speed increases, the frequency and the required excitation capacitance are increased.

At no-load, the terminal voltage and the frequency could not be maintained constant at the same time but only one variable could be maintained constant and the other changes according to the value of the operating speed. But if the operating speed could be regulated at no-load, the terminal voltage and the frequency could be maintained constant simultaneously.

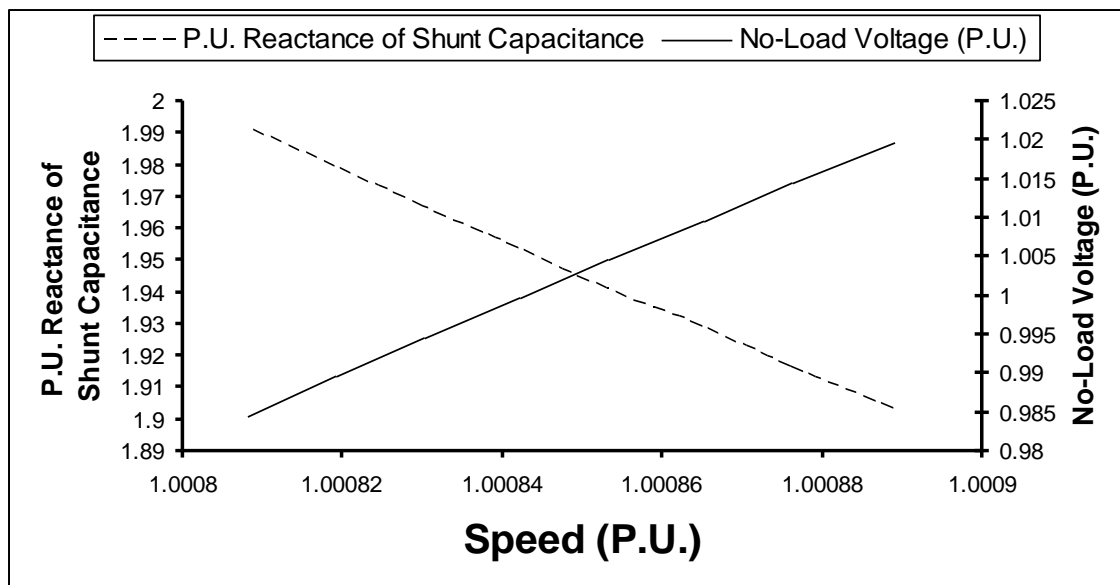


Fig. (4). No-load voltage and excitation capacitance versus speed at $a=1.0$ p.u.

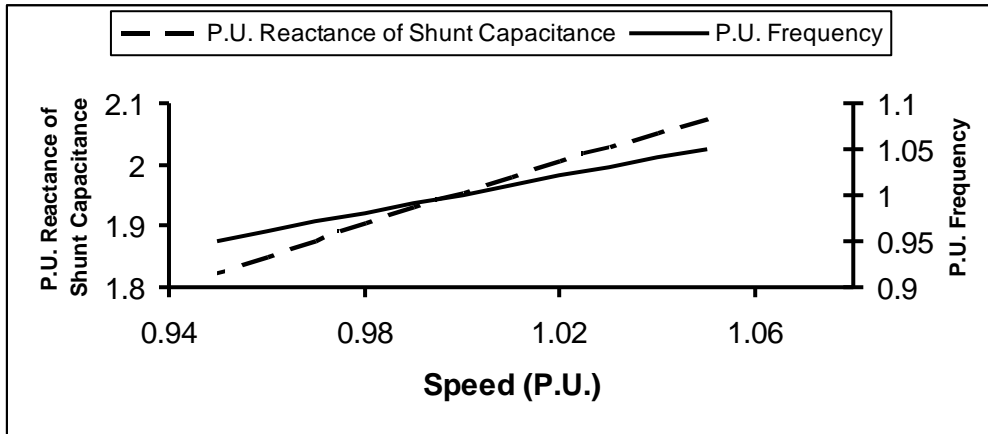


Fig. (5). No-load frequency and excitation capacitance versus speed at $V_m=1.0$ p.u.

3.2 On-load conditions

It may not always be feasible to continuously vary the excitation capacitors to cope with changing of the operating conditions, and load may even remain fixed while the machine speed changes. Under such condition it is necessary to investigate the speed limits between which the machine is capable to build up constant terminal voltage and frequency for given load conditions.

Figures (6) and (7) present the plots of speed limits as a function of load current, at different values of load power factor. From these figures it is seen that the existing speed range shrinks with the increase of the load power factor.

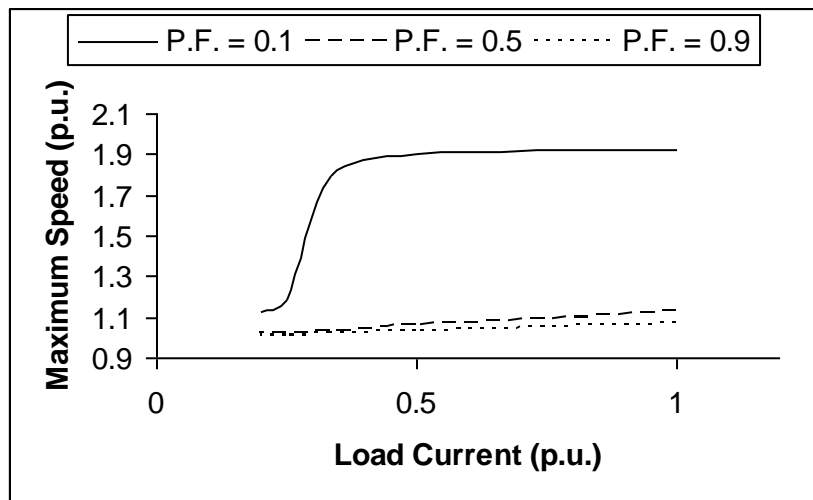


Fig. (6) Maximum speed versus load current, at different values of load power factor.

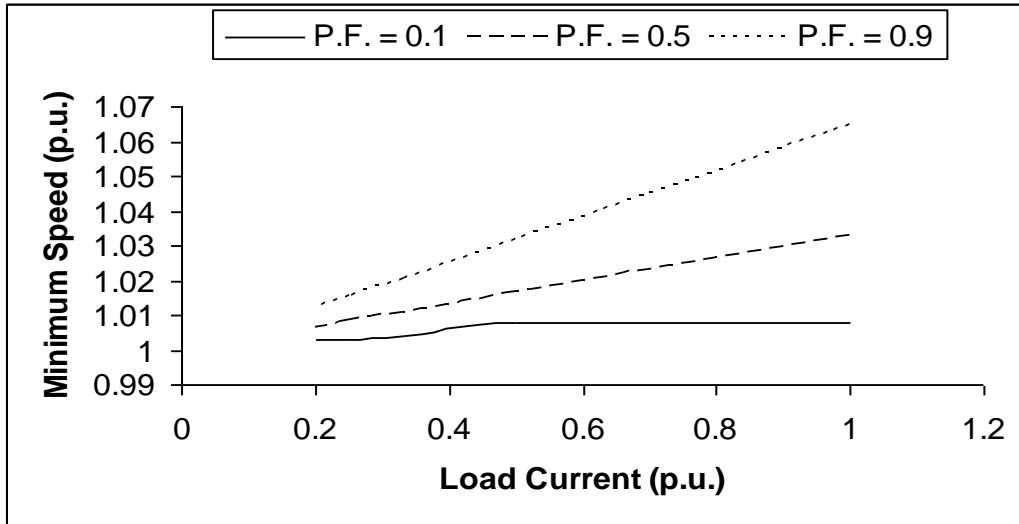


Fig. (7). Minimum speed versus load current, at different values of load power factor.

Figures (8) and (9) present the plots of speed limits as a function of load power factor, at specific values of load current. From these plots it is clearly that, the values of the minimum and maximum speeds increase with the increasing of load current.

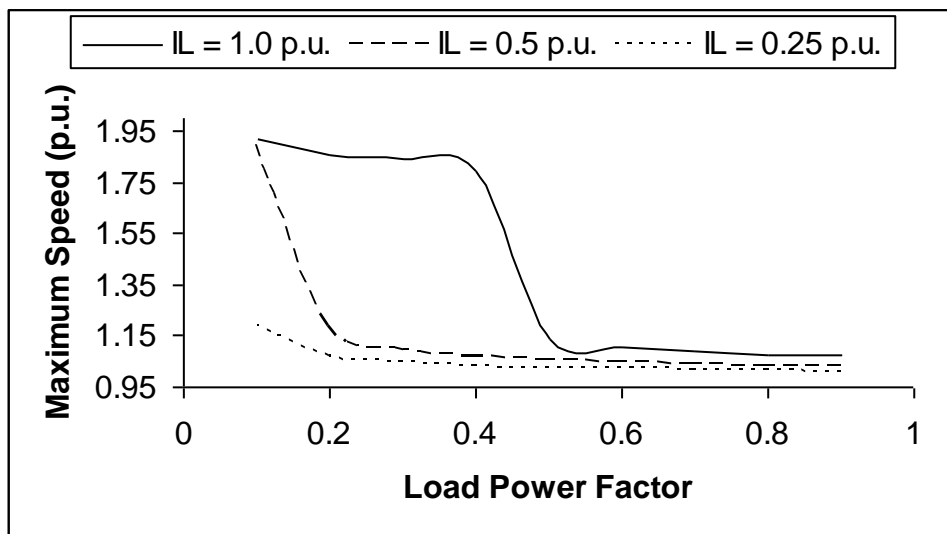


Fig.8: Maximum speed versus load power factor, at different values of load current.

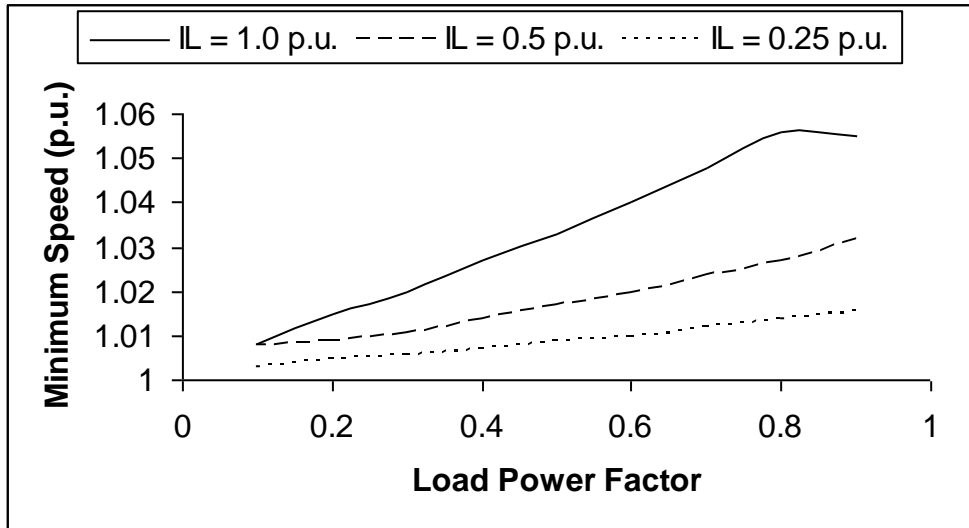


Fig. (9). Minimum speed versus load power factor, at different values of load current.

For any speed within the speed limits, self excitation could be sustained with constant rated values of the terminal voltage and frequency. To maintain the terminal voltage and frequency constant through these ranges, the set of capacitors (shunt and series capacitors) will be calculated using the proposed technique. Figures (10-13) give the required values of shunt and series capacitances versus the operating speed at different load conditions.

It is observed that the shunt capacitance decreases and the series capacitance increases as the load power factor decreases at same load current. And it may also be observed from these figures that the shunt capacitance and the series capacitance increase as load current decreases at same load power factor.

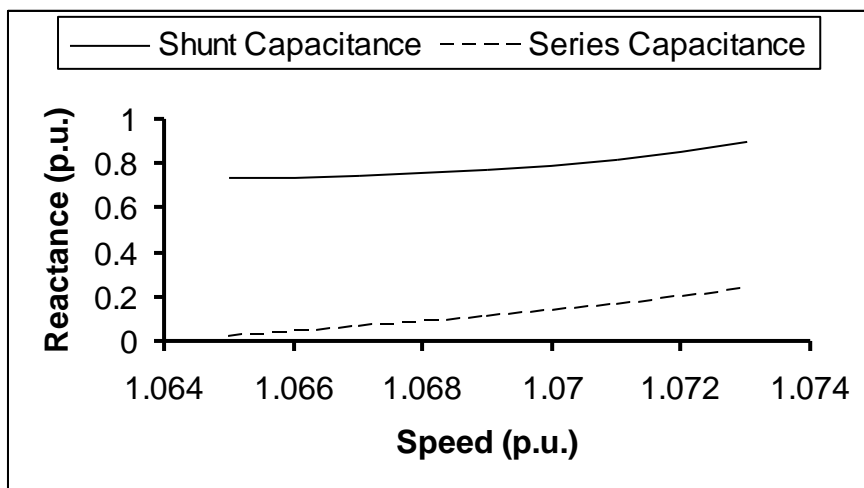


Fig. (10). Shunt and series capacitors versus speed ($V_L=1.0$ p.u., $I_L=1.0$ p.u., $a=1.0$ p.u., P.F.=0.9).

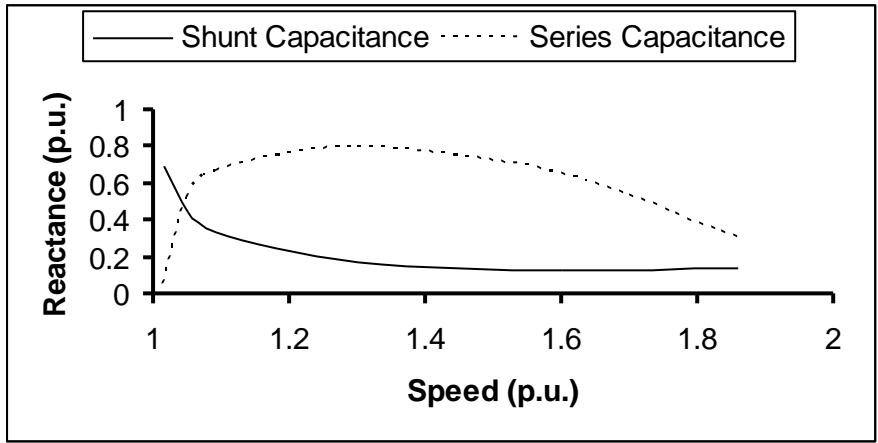


Fig. (11) Shunt and series capacitors versus speed ($V_L=1.0$ p.u., $I_L=1.0$ p.u., $a=1.0$ p.u., P.F.=0.2).

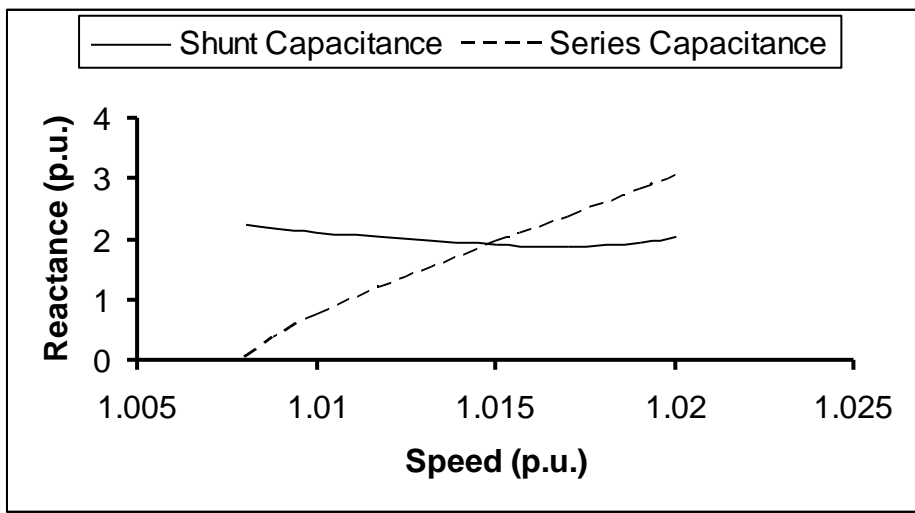


Fig. (12). Shunt and series capacitors versus speed ($V_L=1.0$ p.u., $I_L=0.2$ p.u., $a=1.0$ p.u., P.F.=0.6).

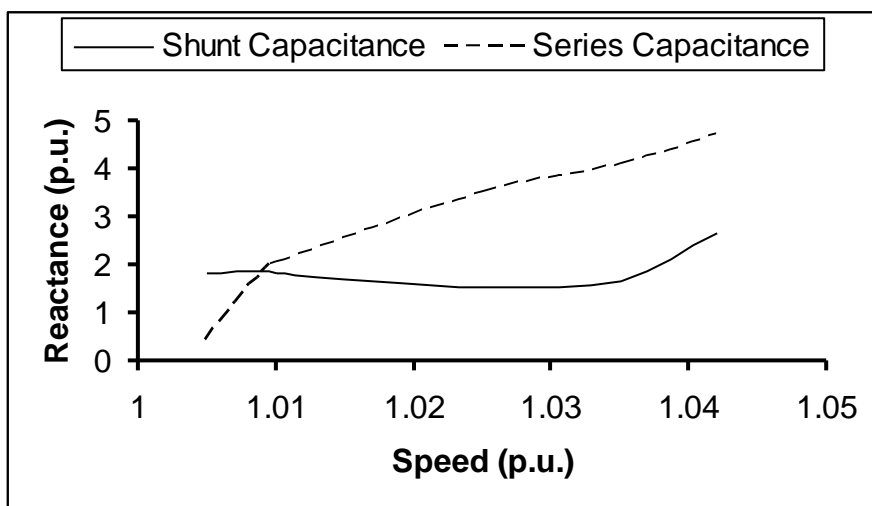


Fig. (13). Shunt and series capacitors versus speed ($V_L=1.0$ p.u., $I_L=0.2$ p.u., $a=1.0$ p.u., P.F.=0.3).

4. Conclusion:

In this paper the short shunt self exciting induction generator has been studied in detail and a suitable methodology has been developed. A new technique to analyze the steady-state behavior of the SESSIG with unregulated prime mover is presented to maintain both of the terminal voltage and frequency at constant rated values. It is found that to maintain both of the terminal voltage and frequency at constant rated values there are ranges of the operating speed, which are different according to the values of load current and power factor. The required set values of capacitors (shunt and series) have been calculated at different load conditions and operating speed by using simple iterative technique. The paper also introduces a new simple and direct method of finding the minimum capacitance required for self-excitation at no-load conditions with the variation of the operating speed.

5. References

- [1] Novotny, D.W., Gritter, D.J. and Studtmann, G.H. "Self Excitation in Inverter driven Induction Machine", *IEEE Transactions on power Apparatus and system*, Vol. PAS-96, No.4, (July August 1977), pp.1117-1125.
- [2] Arrillaga, J. and Watson, D.B., "Static Power Conversion from Self Excited Induction Generators", *Proc. IEEE*, vol. 125, No. 8, (August 1978), pp.743-746.
- [3] Murtuy, S.S., Malik, O.P. and Tandon, A.K., "Analysis of Self Excited Induction Generators", *IEE Proc.*, Part C, Vol. 129, (November 1982), pp. 260-265.
- [4] Elder, J.M., Boys, J.T. and Wood Ward, J.L., "Process of Self Excitation Induction Generator", *IEE Proc.*, Part B, Vol.130/2, (March 1983), pp. 103-108.

- [5] Raina, G. and Malik, O.P. "Wind Energy Conversion Using a Self Excited Induction Generator", *IEEE Transactions on Power Apparatus and Systems*, Vol. PAS-102, No. 12, (December 1983), pp. 3933-3936.
- [6] Rantham C. G, Sutan, D. and Mismail, B., "Steady-State and Transient Analysis of Self Excited Induction Generators", *IEE Proc.*, Part. 8, Vol.136, No.2, (1989), pp. 61-68.
- [7] Tandon, A.K., Murthy, S. S. and Berg, G.J., "Steady-State Analysis of Capacitors Self –Excited Induction Generators", *IEEE Transactions on Power Apparatus and System*, Vol. 103, (1984), pp. 612-618.
- [8] Malik, N. and Mazi, A. "Capacitance Requirement for Isolated Self-Excited Induction Generator", *IEEE Transactions on Energy Conversion*, Vol. EC-2 No. 1, (1987), pp. 62-69.
- [9] Jabri, A. k. and Alolah, A. I., "Capacitance Requirement for Self-Excited Induction Generator", *IEE Proc.*, Part. B, Vol. 137, No. 3, (1990), pp. 154-164.
- [10] Chan, T.F., "Capacitance Requirements of Self-excited Induction Generators", *IEEE Transactions on Energy Conversion*, Vol. 8, No. 2, (June1993), pp. 304 -311.
- [11] Chan, T.F., "Steady-State Analysis of Self-Excited Induction Generators", *IEEE Transactions on Energy Conversion*, Vol. 9, No. 2, (June 1994), pp. 288 -296.
- [12] Chan, T.F. "Analysis of Self-Excited Induction Generations Using an Iterative Method", *IEEE Transactions on Energy Conversion*, Vol. 10, No. 3, (September 1995), pp. 502 -507.
- [13] Shridhar L., Bhim Singh and Jha, C.S., "A Step towards Improvements in the Characteristics of Self Excited Induction Generator", *IEEE Transactions On Energy Conversion*, Vol. 8, No. 1, (March 1993), pp. 40-46.
- [14] Shridhar, L., Singh, B., Jha, C. S., Singh, B. P. and Murthy, S. S., "Selection of Capacitors for the Self Regulated Short Shunt Self Excited Induction Generator", *IEEE Transactions on Energy Conversion*, Vol. 10, No. 1, (March 1995), pp. 10 -17.
- [15] Bim,E. J., zajner S and Burian, Y. "Voltage Compensation of an Induction Generator with Long Shunt Connection", *IEEE Transactions on Energy Conversion*, Vol. EC-4, (1989), pp. 526 -530.
- [16] Malik, N. H. and Haque, S. E., "Steady State Analysis and Performance of an Isolated Self-Excited Induction Generator", *IEEE Transactions on Energy Conversion*, EC-1, No.3, (September 1986), pp. 133 – 139.

APPENDIX A

A 3-phase squirrel cage induction machine is selected for computation. The electrical details and parameters of the machine are as below:

Rating: 3.7 KW, 415 Volts, 7.6 Amps, 4-pole.

Stator connection: Delta

Frequency: 50 HZ

Stator resistance: $r_s=0.053$ p.u.

Rotor resistance: $r_r=0.061$ p.u.

Leakage reactance: $x_s=x_r=0.087$ p.u.

Base impedance: 94.58 ohms/phase

Constants of saturation c/c: $K_1=1.6275$, $K_2=0.3418$

التحكم في جهد و تردد المولد الحثي ذاتي الإثارة

حنفي حسن حنفي حسن احمد محمود جسرهما محمد ممدوح عبد العزيز

احمد فهيم زوبع

قسم القوى والآلات الكهربائية- كلية الهندسة- جامعة القاهرة
(قدم للنشر في 2007/10/18؛ وقبل للنشر في 2008/3/24)

ملخص البحث.

A New Image Steganography Technique

Ahmed A. Abdelwahab

Electrical Engineering Department, College of Engineering

Qassim University, Qassim, KSA

abdelwahab@qec.edu.sa

(Received 27/2/2008; accepted for publication 17/5/2008)

Abstract

A new image steganography technique is proposed by employing block matching process. The subject secret image which needs to be transmitted, without noticing its existence, is vector-quantized using a lookup vector-table which is directly formed from another image called the host (key) image. The address vector which contains the addresses of the chosen vectors of the lookup table can then be reordered in secret permutation resulting in a permuted address vector (PAV). This secret permutation (SP) is the secret key for the image steganography process. During this proposed steganography process, nothing is embedded in the key image which could be any image. The proposed scheme can be applied in spatial domain as well as in the approximation subband image of one level discrete wavelet transform decomposition in order to achieve both much smaller lookup table size and less processing time. The simulation of the proposed image steganography technique shows that the extracted subject secret image has good quality even after common signal processing operations on the key image. Moreover, the key image can be as small as one fourth of the subject secret image and high acceptable quality of extracted secret image can still be obtained.

Key words: Image Steganography, Block Matching, Vector Quantization, Secret Permutation, Discrete Wavelet Transform and Information Confidentiality.

1. Introduction

A plaintext message may be hidden in one of two ways. The techniques of steganography conceal the existence of the message, whereas the techniques of cryptography render the message unintelligible to outsiders by various transformations of the text. While cryptography is about protecting the content of messages, steganography is about concealing their very existence. It comes from Greek words literally means covered or hidden writing [1], and is usually interpreted to mean hiding information in other information. Examples include

sending a message to a spy by marking certain letters in a newspaper using invisible ink, and adding sub-perceptible echo at certain places in an audio recording. Secret information can be embedded inside a piece of unsuspecting information and transmitted without noticing the existence of the transmitted information. Information encryption techniques are different from those of information steganography. The later hides the information in an intellectual text using an algorithm and a secret key while the former hides the information by generating a ciphertext which is not an intellectual text using an algorithm and a secret key. It should be computationally infeasible to decrypt the cipher information, even if the information encryption algorithm is known as long as the key is kept secret [2]. Secret symmetric key based information steganography techniques provide information confidentiality and sender authentication which have many important applications in intelligent and military communications as well as in civil communications for economic, industrial or scientific secret information exchanges over an open environment such as the internet. In [3], Yu-Chen suggested a grayscale image hiding scheme that is capable of hiding multiple secret images into a host image of the same size. The secret images to be hidden are first compressed by vector quantization with additional index compression process. Then, the compressed secret images are encrypted and embedded into the least-significant bits of the host pixels. In [4], Suk-Ling et al proposed an image-hiding scheme by exploring the block correlation between the cover-image and the secret-image.

In this paper, a new image steganography algorithm is proposed by using a block matching technique between the secret image and a key image and a symmetric secret key is produced. For most applications, digital image steganography schemes must be designed such that the secret image can be extracted reliably in recognizable version after common signal processing operations on the key image, and in some cases, even after deliberate attacks for a robust image steganography technique.

Section 2 provides a background of the tools used in the proposed technique; the proposed image steganography technique is explained in section 3 while the computer simulation results for the proposed technique in both spatial domain and transform domain are included in section 4. Section 5 concludes the paper.

2. Background

Vector quantization is a very powerful technique in image coding where both the transmitter and the receiver have the same codebook which needs no transmission [5-6]. Vector quantizing an input image consists of finding the addresses (indexes) of the best

representative codevectors in the codebook to the input image vectors taken in normal scanning sequence (from left to right and from top to bottom). These codebook addresses constitute the address vector (AV) of the encoded image. Transmitting the AV to a receiver having the same codebook, the image can be easily decoded and reconstructed. The reconstructed image quality depends on the codebook design. Since our prime interest in this paper is that the secret image can be extracted reliably in recognizable version, the codebook is replaced by a lookup vector-table formed directly from the key (host) image without using any codebook design algorithms. Simply speaking, all the key image vectors are taken as codevectors constituting the lookup vector-table. Because of the high similarity between images, a good quality image can still be reconstructed from this simple codebook if the size of the image vector is as small as 2x2. The size of the lookup vector-table which depends on both the chosen size of the codevector (n x n) and the size of the key image (N x N) will be $[(N \times N) / (n \times n)]$ codevectors.

Image decomposition using the 2-dimensional discrete wavelet transform (2-d DWT) is a well known technique in image processing which classifies the image information into four subband images, each with size of one fourth of the original image. Namely the four subband images are called LL, LH, HL and HH respectively shown in figure (1).

LL subband image is the approximation subband image while the other three subband images have edge information (Horizontal, vertical and diagonal respectively) in the image content [6-7]. A good quality recognizable image can still be obtained by setting the three subband images LH, HL and HH to zeros and using the 2-d inverse DWT (2-d IDWT) of the only nonzero LL subband image.

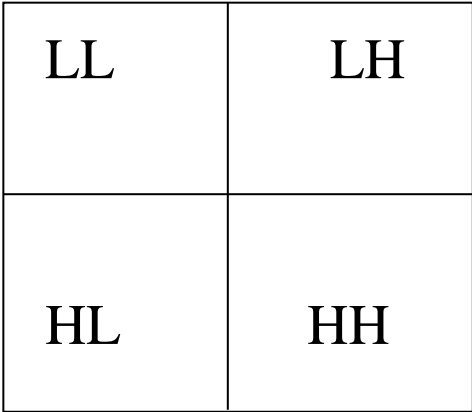


Fig. (1). One level 2d-DWT decompositions subbands

3. The Proposed Image Steganography Technique

The proposed scheme exploits the large similarities among different images. The key image of size $(N \times N)$ can be divided into small blocks of dimension $(n \times n)$ which constitute the key image lookup vector-table of size $[(N \times N) / (n \times n)]$ without using any codebook design algorithms. The subject secret image is also divided into $(n \times n)$ blocks and vector-quantized using the key image lookup vector-table. The address vector which contains the addresses of the chosen vectors of the lookup table can then be reordered in secret permutation resulting in a permuted address vector (PAV). This secret permutation (SP) is the secret key for the proposed image steganography process. The end users should agree –in secret- on the key image which could be any image such as a screen saver image so that the key image even needs not to be transmitted. The receiver could build a similar lookup vector-table and reconstruct the subject secret image from the received PAV and SP vectors. Moreover, the key image could be considered as another secret key between the end users. This spatial based scheme has a potential disadvantage that the size of both PAV which depends on the size of the subject secret image and the lookup vector-table which depends on the size of the key image could be quite large. Although, the lookup vector-table needs not to be transmitted, a smaller lookup vector-table size would reduce the image steganography process time which includes the key image lookup vector-table generation, the subject secret image vector quantization search time and the generation of the corresponding PAV and SP vectors. Moreover, a smaller lookup vector-table size would also reduce the lookup vector-table required memory size as well as the subject secret image extracting (reconstruction) process time.

Therefore, this scheme can be applied in more efficient way in the 2-d DWT subbands. One-level decomposition of the 2d-DWT for both the key (host) image and the subject secret image is used. The lookup vector-table is formed from the approximation subband (LL) of the key image and hence the lookup vector-table becomes much smaller in size. Only the approximation subband LL of the subject secret image is then vector quantized and hence the address vector becomes much smaller in size. The sender generates the corresponding PAV and SP vectors and sends them to the receiver as the secret key via a secure channel. The receiver can reconstruct the approximation subband LL of the subject image from the LL subband of the key image lookup vector-table using the received PAV and

SP vectors. The receiver could set the other edge subbands (LH, HL and HH) to zeros and extract a good recognizable version of the subject secret image by the 2-d IDWT.

For the objective evaluation of the reconstructed subject secret image of size (K x L), the peak signal-to-noise (PSNR) in dB is defined in equation 1.

$$PSNR = 20\log_{10}\left(\frac{255}{RMSE}\right) \text{ dB} \quad (1)$$

Where

$$RMSE = \sqrt{\frac{1}{KxL} \sum_i (X_i - Y_i)^2}$$

X_i and Y_i are the values of the original and reconstructed image pixels respectively, KxL is the total number of pixels of the secret image and i runs over all secret image pixels.

4. Computer simulation results for the proposed technique

Two gray images Lena of size 512x512 pixels and Peppers of size 256x256 pixels are used as key images. The size of the subject gray secret image used with Lena image is 112x92, while the one used with Peppers image is Elaine image of size 512x512. The first set of images is shown in figure (2) while figure (3) shows the second set of images which indicate that the proposed technique works well even if the key image is one fourth of the secret image.

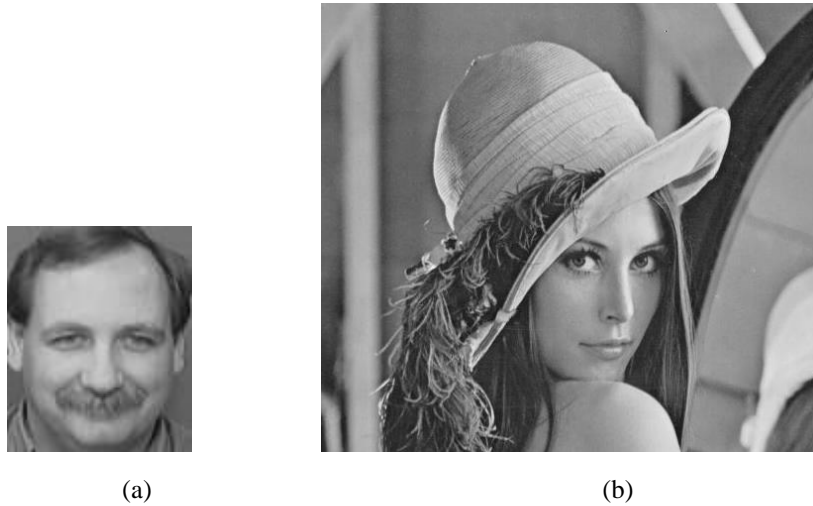


Fig. (2). First set original images (a) 112x 92 subject secret image (b) 512x512 key Lena image

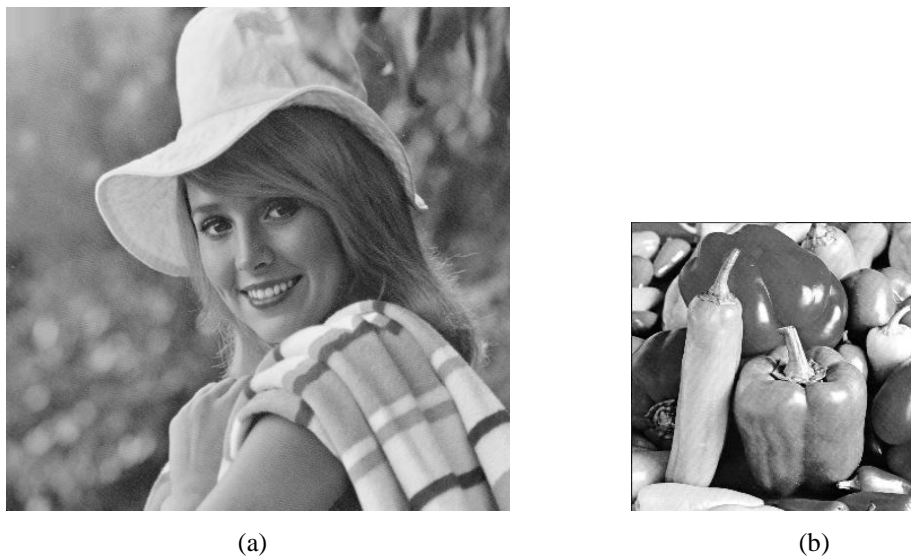


Fig. (3). Second set original images (a) 512x512 secret image Elaine (b) 256x256 key image Peppers

4.1. Spatial based proposed scheme for image steganography.

Using the first set of images of figure (2), the block size is chosen to be 2x2 which generates a key image lookup vector-table of size 65536 with four pixels per row. Thirty minutes and 20 seconds is the elapsed time at the transmitter for the subject secret image vector quantization process in order to generate the corresponding PAV and SP vectors using Matlab on PC Pentium III 866 MHz, while at the receiver the elapsed time for the secret image extraction process using the received PAV and SP vectors of size 2576 each is 18 minutes and 37

seconds. The extracted subject secret image is indistinguishable from the original one with PSNR = 44.23 dB.

The memory size of the lookup vector-table is $65536 * 4 * 8 = 2,097,152$ bits while that of the PAV vector is $2576 * 16 = 41216$ bits and that of SP vector is $2576 * 12 = 30912$ bits.

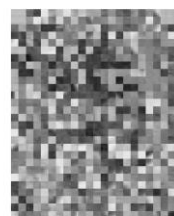
Therefore, the total memory size needed is $2,169,280$ bits = 271.160 KB. The two vectors PAV and SP are transmitted along with the name of the key image with bit rate of $72128/(112*92) = 7$ bpp. The bit rate can be reduced if the sender decides to encrypt the address vector (AV) instead of using the secret permutation step. Hence the bit rate becomes $41216/(112*92) = 4$ bpp.

These previous figures would be changed if the block size is changed to 4x4. Table 1 compares the results of the spatial based proposed scheme. Table 1 shows that increasing the block size four times has decreased the bit rate by 78.6% and the processing time by 78.4% but PSNR of the extracted secret image is reduced by about 27%. Figure (4-a) shows the extracted subject secret image quality if 4x4 block-size is used.

The subject image can't be revealed if the key image is unknown. Figure (4-b) shows the extracted secret image if another key image is used with the correct PVA and SP vectors. In order to reduce the lookup vector-table memory size and the processing times, next section shows the results of the DWT based proposed scheme.

Table 1: Results for different block size in spatial based proposed scheme using first set images

Block size	Total memory size lookup vector- table +PVA+SP KB	Bit rate bpp	Encryption elapse time minutes	Extraction elapse time minutes	PSNR dB
2x2	271.160	7	30.33	18.60	44.23
4x4	264.076	1.5	6.55	4.0	32.26



(a) Using the correct key image (PSNR=32.26 dB) (b) Using an incorrect key image

Fig. (4). Extracted subject secret image using spatial based proposed scheme using 4x4 block size

4.2. DWT based proposed scheme for image steganography.

One-level decomposition of the 2d-DWT for both the key image and the subject secret image is performed. The lookup vector-table is formed from only the approximation subband of the key image. Using a block size of 2x2 and a key image of size 512x512, the approximation subband LL lookup vector-table size will be 16384 with four coefficients per row (size of $LL_{key} = 256 \times 256$). For a subject secret image of size 112x92, the length of each of the vectors PAV & SP will be reduced to only 644 (size of $LL_{secret} = 56 \times 46$). Therefore, the bit rate and the processing time have dramatically reduced. Table 2 compares the results of the DWT based proposed scheme. Table 2 shows that increasing the block size four times, has further decreased both the bit rate and the processing time but on the expense of the extracted secret image quality which is reduced by about 17.27%. Note that the size of the subject image is taken as 112x88 in order to take the block size of 4x4 in the approximation subband of the subject secret image (size of $LL_{subject} = 56 \times 44$). Hence, the lookup vector-table size will equal to 4096 with 16 coefficients per row and the length of each of the vectors PAV & SP will be 154. Figure (5) shows the DWT based extracted secret subject images quality.

Table 2: Results for different block size in DWT based proposed scheme

Block size	Total memory size lookup vector-table +PVA+SP KB	Bit rate bpp	Encryption elapse time minutes	Extraction elapse time minutes	PSNR dB
2x2	67.468	1.5	1.4	0.746	32.41
4x4	65.921	0.3125	0.347	0.21	26.82



(a) 2x2 block size (PSNR=32.41 dB) (b) 4x4 block size (PSNR=26.82 dB)

Fig. (5). Extracted secret images using DWT based proposed scheme

Using the second set of images of figure (3), one-level decomposition of the 2d-DWT for both the key image and the subject secret image is performed. The lookup vector-table is formed from only the approximation subband of the key image. Using a block size of 2x2 and

a key image of size 256x256, the approximation subband LL lookup vector-table size will be 4096 with four coefficients per row (size of $LL_{key} = 128 \times 128$). For a subject secret image of size 512x512, the length of each of the vectors PAV & SP will be 16384 (size of $LL_{secret} = 256 \times 256$). The bit rate can be calculated as $[16384 \times (12 + 14)] / (512 \times 512) = 1.625$ bpp. Only 29.75 seconds is the elapsed time at the transmitter for the subject secret image vector quantization process in order to generate the corresponding PAV and SP vectors using Matlab on Toshiba laptop Centrino Duo processor 1.83 GHz, while at the receiver the elapsed time for the secret image extraction process using the received PAV and SP vectors of size 16384 each is only 3.985 seconds.



Fig. (6). Extracted secret image Elaine using DWT based proposed scheme 2x2 block size (PSNR=33.95 dB)

Figure (6) shows the extracted secret image Elaine with good quality of 33.95 dB.

The receiver can still extract the subject secret image even if the used key image at the receiver is in bad shape (noisy, compressed, cropped, etc). Figure (7-b) shows the extracted secret image if the receiver has to use only three quarters of the original key image. The upper left quarter of the key image is missed as shown in figure (7-a). 6.25% randomized zeros are introduced to the key image shown in figure (8-a) and the extracted secret image still has acceptable quality of PSNR=21.47dB as shown in figure (8-b). Using the key image with 10 % Gaussian noise added at the receiver shown in figure (9-a), the extracted secret image is still recognizable with PSNR = 24.87 dB as shown in figure (9-b).



(a)



(b)

Fig. (7). (a) Key image with missing upper left quarter (b) Extracted secret image using 2x2 block size in DWT based proposed scheme (PSNR=12.52 dB)



(a)



(b)

Fig. (8). (a) Key image with randomized zeros (6.25%) (b) Extracted secret image using 2x2 block size in DWT based proposed scheme (PSNR=21.47dB)



(a)



(b)

Fig. (9). (a) key image with 10% Gaussian noise added. (b) Extracted secret image using 2x2 block size in DWT based proposed scheme (PSNR=24.87 dB)

5. Conclusions

A new robust technique for image steganography is proposed in this paper. A lookup vector-table is directly formed from a key (host) image and used to vector-quantize the subject secret image and produce an address vector. A secret permutation of the address vector is the secret key for the image steganography process. Unlimited number of subject secret images, each with a different secret key, can be encrypted using a single key image. The subject secret image can be as large as four times the key image and high acceptable quality of extracted secret image can still be obtained. The proposed technique does not optimize the used lookup vector-table so that the receiver can generate an exact copy of it in much less time without the need of transmitting the lookup vector-table itself. However, the transmitter is advised to use a key image which is highly correlated with the secret subject image as much as possible. This scheme can be applied in spatial domain and in a more efficient way using one level of the 2-d DWT subbands and a recognizable version of the secret image can still be obtained. The computer simulation of the proposed image steganography technique shows that the extracted subject secret image has good quality even after common signal processing operations on the key image.

6. References

- [1] Johnson, N.F., Duric, Z., and Jajodia, S., *Information Hiding: Steganography and Watermarking-Attacks and Countermeasures*, Kluwer Academic Publishers, Third Printing, 2003.
- [2] Stallings, William, *Cryptography and Network Security: Principles and Practices*, Prentice-Hall, Third Edition, 2003.
- [3] Hu, Yu-Chen, "High-Capacity Image Hiding Scheme Based on Vector Quantization," *ScienceDirect, Pattern Recognition*, Volume 39, Issue 9 , (2006), pp. 1715-1724.
- [4] Li, Suk-Ling, Leung, Kai-Chi, Cheng, L.M. and Chan, Chi-Kwong, "A Novel Image-Hiding Scheme Based on Block Difference," *ScienceDirect, Pattern Recognition*, Volume 39, Issue 6 , (2006), pp. 1168-1176.
- [5] Gray, R.M. and Gersho, A., *Vector Quantization and Signal Compression*, Norwell, MA: Kluwer, 1992.
- [6] Cosman, P.C., Gray, R.M., and Vetterli, M. "Vector Quantization of Image Subbands: a Survey," *IEEE Trans. on Image Processing*, Vol. 5, No. 2, (1996), pp. 202-225.
- [7] Mallat, S. G., "A Theory for Multiresolution Signal Decomposition: The Wavelet Representation," *IEEE Trans. on Pattern Analysis and Machine Intelligence*, Vol.11, No.7, (1989), pp. 674-693.

طريقة جديدة لإخفاء الصور الرقمية
أحمد عادل عبد الوهاب
قسم الهندسة الكهربائية- كلية الهندسة- جامعة القصيم
القصيم، المملكة العربية السعودية
(قدم للنشر في 2008/2/27؛ وقبل للنشر في 2008/5/17)

ملخص البحث. هذا البحث يقترح طريقة جديدة لنقل الصور الرقمية خفية وذلك بمقارنة بيانات الصورة المراد نقلها سراً ببيانات صورة عامة متفق عليها سراً. المفتاح السري لخوارزم التخفي المقترح للصورة السرية الرقمية هو تبديل لعناوين متجهات الصورة السرية في جدول متجهات الصورة العامة، واستخدام طريقة المحدد الاتجاهي في المقارنة، وإعادة تركيب الصورة السرية من الصورة العامة باستخدام المفتاح المرسل. يمكن تطبيق هذا الخوارزم في مجال الصورة الفراغي أو في مجال تحويل الموجة لتقليل البيانات المرسله للمفتاح السري و تقليل حجم الذاكرة المطلوبة وكذلك تقليل زمن العمليات. بتطبيق هذا الخوارزم أمكن الحصول علي الصورة السرية من الصورة العامة المتفق عليها باستخدام المفتاح السري بجودة جيدة ومقبولة حتى بعد تعرض الصورة العامة لبعض عمليات التشويه و الشوشرة.

SPACE COORDINATES OF COMPUTER MODEL'S DETAILS USING DIGITAL CLOSE-RANGE PHOTOGRAMMETRY

Ahmed A. ELSONBATY⁽¹⁾ & Mostafa A-B EBRAHIM⁽²⁾

(1) Associate t Professor at Qassim University, Civil Eng. Dept., Saudi Arabia

(2) Associate Professor at Assiut University, Civil Eng. Dept., Egypt

(Received 15/4/2008; accepted for publication 30/4/2008)

e-mails??????????????

Abstract

3D object animation could be very useful for obtaining the space coordinates of the computer model's points. Computer model's points consist of two categories of points. The first contains the points that have been used to create the computer model. The second is the points lie on the model's surfaces but have unknown coordinates.

Creating 3D computer models can be done using the obtained space coordinates from the photogrammetric measurements. Once the 3D computer model has been created, different measurements can be done from this model, but just for the points belonging to the first category. Measuring the space coordinates for the points of second category needs establishing of a new measuring technique. This new method will use 3D object animation technique together with the digital close-range photogrammetric techniques.

The visible and hidden parts of the 3D computer model play an important role in finding the space coordinates of the surface details. Once the hidden surfaces were excluded of the scene, it will be easy to determine the space coordinates of the points lying among the nearest model's points of the surface. The method depends on model animation which changes the position of the surfaces during the motion. During the animation, the model's surfaces will change its position, from visible to hidden and vise versa depending on their points' space coordinates. Method will be explained intensively through this paper.

Keywords: 3D computer modeling, close-range photogrammetry, central projection, computer graphics.

Introduction

It is well known that digital photogrammetry is one of the most important measuring techniques that have been used in documentation of architectural historical building

and world heritage [1][6]. In 1996 Hanke K. and Ebrahim M. have presented a new approach called "Digital Projector" that can be used in documenting the historical buildings and monuments in their real shape and dimensions. The documentation is in the form of 3D

computer models. Full measurements can be done for the obtained computer model, but just for the points that have been used in creating the computer model. What about the other points that lie on the computer models' surfaces but not included in creating the model?

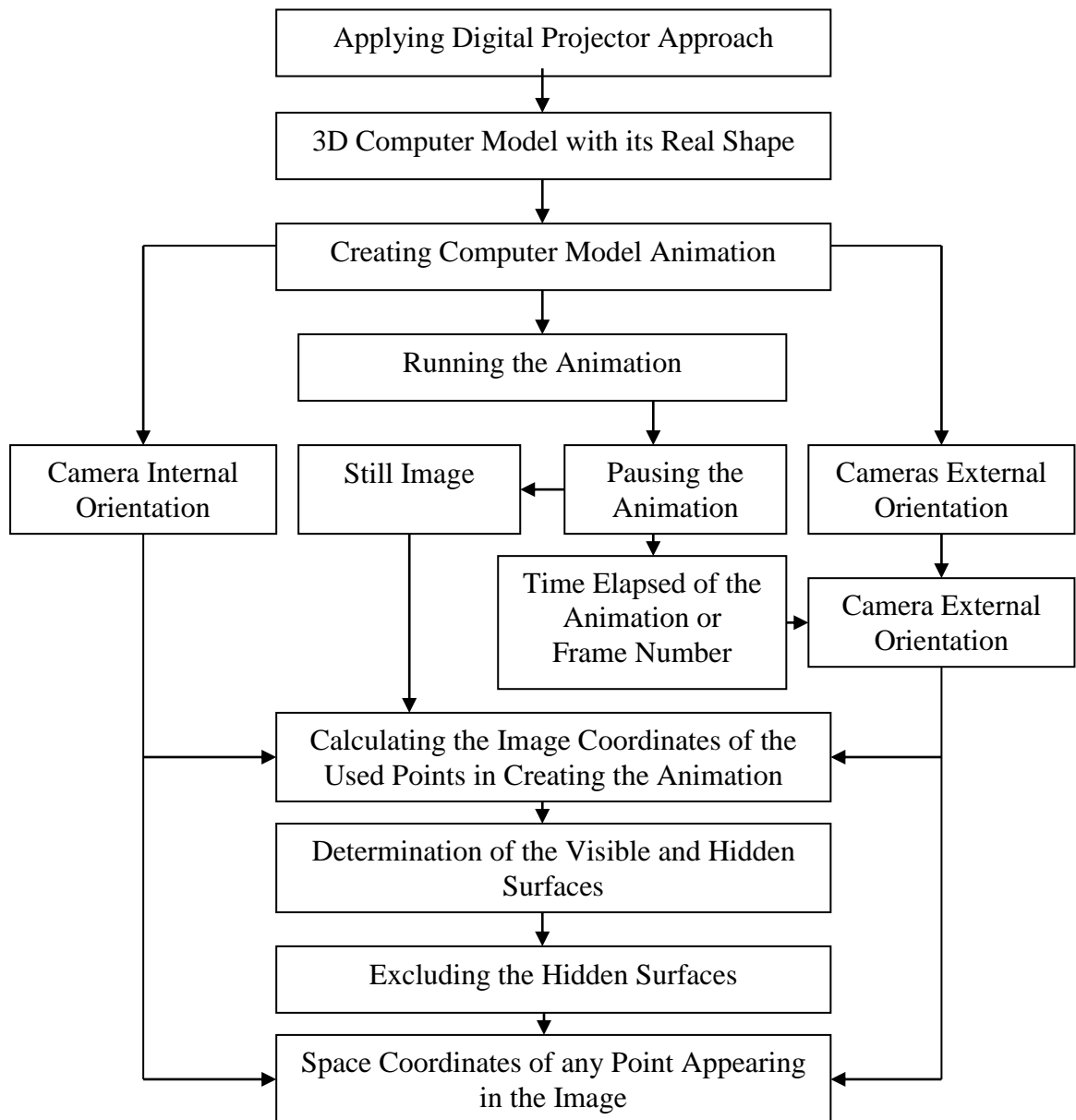


Fig. (1). System Scheme Chart.

It is a very important question that will be answered through this research work. Figure (1) shows the scheme chart that will be followed through this research. This chart will follow the digital projector approach technique as it gives 3D computer model with its real shape and dimensions. Once the computer model is created, it can be imported to the 3D Studio software to create the object animation after applying the "Digital Projector Approach". This measuring system is not limited to the "Digital Projector Approach", but can be applied to any 3D computer model animation.

The easiest way to import the 3D computer model to the animation software is using DXF file format. Drawing exchange format files (DXF file) are vector format files designed with vector data interchange in mind but are vendor-controlled and originated as a format supporting a single application. In addition DXF was specifically tailored for CAD information useful in the construction of mechanical, electrical, and architectural drawings. DXF therefore supports not only common vector elements such as circles and polygons, but also complex objects frequently used in CAD renderings, such as 3D objects and hatching. Each DXF consists of five sections: a header; tables; blocks; entities sections and an end-of-file marker. DXF files are very good tools to show the 3D wireframe because they contain points and lines information (Figure 2). As the DXF files contain also the data of the surfaces between the points, rendering and shading can be done to show the surfaces of the 3D model (Figure 3).

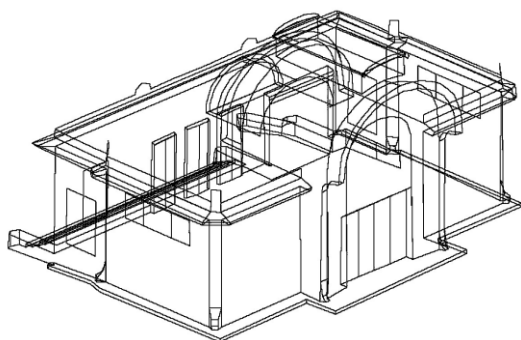


Fig. (2). Computer model Wireframe
(Hidden and Visible surfaces)

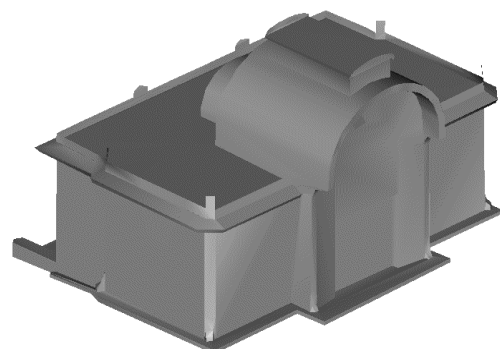


Fig. (3). shaded Computer Model
(Visible Surfaces Only)

Once the computer model has been imported to the animation software, animation of this computer model can be created. There are four basic techniques used in animation:

- Drawn animation
- Cut-out animation
- Model animation or stop motion animation
- Computer animation or computer generated imagery (CGI)

The last technique will be used throughout this work using 3D Studio software. Animation formats have been around for several years. The basic idea is that of the flip-books one played with as a kid. Rapidly display one image superimposed over another to make it appear as if the objects in the image are moving. Very primitive animation formats store entire images that are displayed in sequence, usually in a loop. Slightly more advanced formats store only a single image, but multiple color maps for the image. By loading in a new color map, the colors in the image change and the objects appear to move. Advanced animation formats store only the differences between two adjacent images (called frames) and update only the pixels that have actually changed as each frame is displayed. A display rate of 10-15 frames per second is typical for cartoon-like animation. Video animation usually require a display rate of 20 frames per second or better to produce a smoother motion.

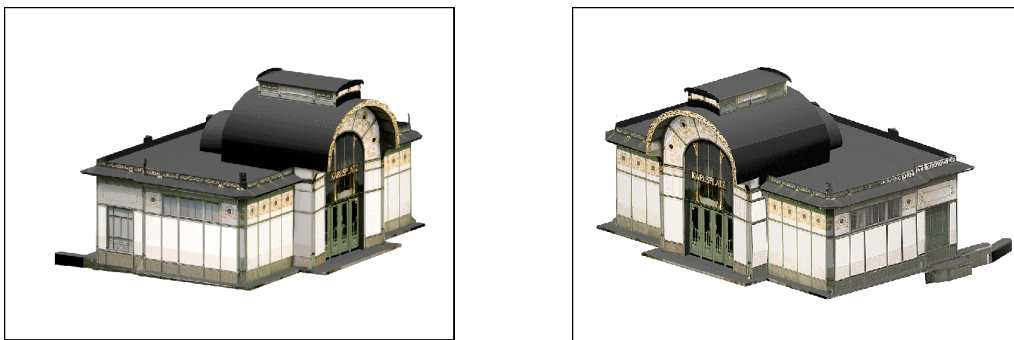


Fig. (4) & (5). Detailed Computer Model

Using animation as a visualization tool, objects can be shown from different direction and point of views (Figure 4 & 5). It runs automatically as it has been created, no control of the object motion unlike the VRML technique which can be manually controlled [5].

Ebrahim, 1998 has explained in details the visualization of the 3D computer model with its real shape and details using the "Digital Projector Approach". He used Otto Wagner's Stadtbahn Station buildings on the Karlsplatz in Vienna as a test field which has been selected in 1990 as a small test object, photographed, measured and documented, in order to get well-checked materials to train students and

photogrammetrists as well as to evaluate internationally the results of the analytic photogrammetric amount of control information. The test object was a masterpiece of Art Nouveau, built in 1898-1899. [9]

Considering an architectural restitution, first a complete reconstruction of the building's shape has to be done using e.g. any digitally matching method (e.g. [8]) or a bundle adjustment program [7] followed by a definition of lines and surfaces in a CAD environment. A few of the already before used images are then chosen to do a "Digital Slide Projection" onto the surface to achieve a restitution of the architectural details on the facades of the building. The surfaces of the different objects are not restricted to planes but were also of regular curved (e.g. cylinder etc.) and even irregular or free formed shape [6].

The space coordinates of the points that have been used to create this model can be easily measured, but the other model details' space coordinates are impossible to be measured unless a certain new method is applied. The idea of this new method will be explained in the next section.

The system idea of the new technique

As mentioned previously, model animation is a kind of presenting sequence of images with a certain speed. The image sequence is depending on the media that has been used to create the animation. As example, to create an animation through 3D studio MAX, a base station for the camera must be defined which determines the camera passes. The number of images that will be created depends on the desired number of frames. The camera internal orientations are be known according to the software options. Each frame will have its camera position, so each camera station has its known external orientations. Running the animation will change the camera external orientation according to the showed frame. Pausing the animation will give the frame number or the elapsed time. Any of these will lead to the camera station with known exterior orientations. As the camera's internal and external orientations are known, any details that appear in the image can be measured. The ability of measuring from a single image can be achieved when an additional condition is considered [3]. This additional condition in our case will be the surface that the desired point is lying on. The system idea of the new technique depends on the 3D computer model data base which contains the space coordinates of the objects' points, the object's edges, and the

object's surfaces information. Using photogrammetric measurements techniques, the space coordinates of the object details can be measured after excluding the information of the hidden part of the surfaces and keeping that of the visible part.

The system calculations

After photogrammetric solution, a data base of the model will be available which contains all information about the object in space (points, lines and surfaces). Also, the camera's internal and external orientations will be known from the paused animation which will depend on the frame number or the elapsed time. The paused image information are:

- 1- The camera internal orientation known from the defined camera.
- 2- The camera external orientation known from frame number.
- 3- The image coordinates of the visible surfaces' points from the object space coordinates and the camera orientation.

Now, the problem can be summarized into the following 3 items:

- [1] Calculation of the image coordinates of the object.
- [2] Which faces of the object are visible.
- [3] Calculating the space coordinates of any point appearing in the image plane.

To solve the above items, the space object has to be represented in a way that gives a complete and unambiguous definition of the object, not only the shape of the boundaries but also the object's interior and exterior regions. In the following section, a brief explanation about the way of representing objects on the computer will be given.

Boundary representation of object

The object in space is enclosed by a set of faces, which form a closed and oriental surface. This guarantees that it is possible to distinguish between the interior and exterior region [4]. The orientation is usually established by the direction of a normal vector. This means that the boundary is determined by a set of faces bounded by one or more rings (*loops* consisting of edges and vertices). So, the object in space is approximated into a polyhedron.

Data Structure

The boundary of each polyhedron consists of three types of geometric elements: Vertices (V), edges (e) and faces (f). Each vertex bounds an equal number of edges and faces, each edge is bounded by two vertices and two faces. All these elements can be addressed in the internal data base by pointers. Pointers are not data entities, but an attributes of some data entity [2]. The definitions of the geometric elements are presented in the next subsections.

The points' data structure (Figure 6)

Each point storage has record number of the point (id), Space coordinates of the point (P), Image coordinates of the point (P^C), and address of the next point ($next$)

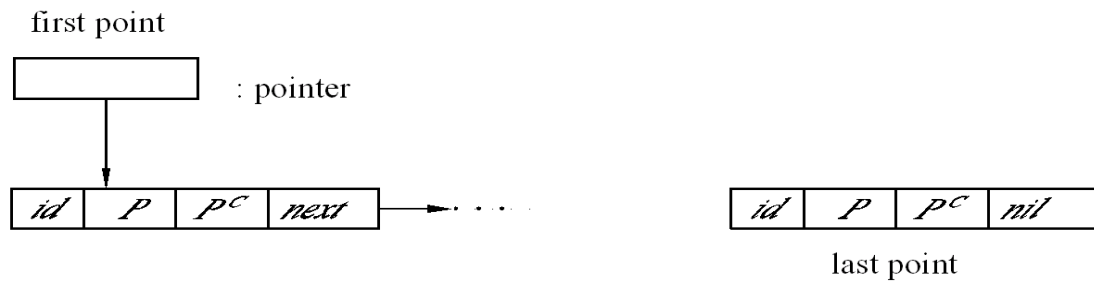


Fig. (6). Points' Data Structure

Edges' data structure (Figure 7)

An edge is a line segment. It joins two points, the initial point i_p and the end point e_p . Therefore the edges data structure will be as follows:

i_p and e_p are the pointer to the initial point and the end point. f_l and f_r are the pointers to the neighboring faces of the edge, one on the left side, one on the right, if seen from outside in the direction i_p-e_p .

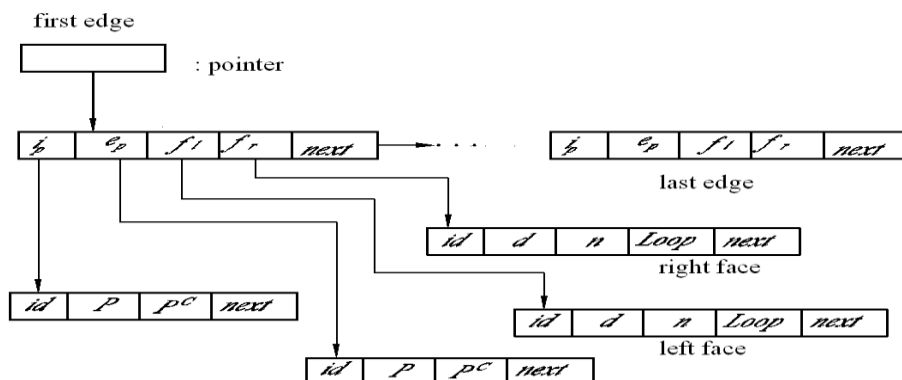


Fig. (7). Edges' Data Structure

Faces' data structure (Figure 8)

The faces of the polyhedron will be defined by a sequence of the included vertices (*loops*). If seen from outside, the outer loop of a certain face will be processed mathematically as positive (*anticlockwise*) order, the inner one will be negative (*clockwise*). So, for each face, the following information will be stored:

The record number of the face (*id*), oriented distance between the face and origin (*d*), the normal vector to the face pointing outside (*n*), the pointer to the list of the bounding polygons of the face (*f_loop*) and pointer to the next face (*next*).

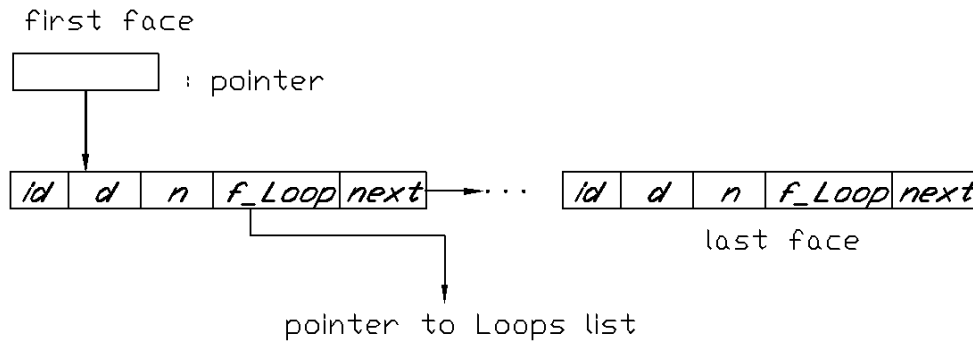


Fig. (8). Faces' Data Structure

Now, a complete database on all objects in space (*points, edges and faces*) is available. Assuming that, the image for that object is obtained from the paused animation with known camera exterior and interior orientations (*camera station and image plane p*)).

Next, we are going to discuss the two important items which fulfill the main aim of this paper::

- Formation of a list of faces that will appear in the image plane.
- Calculation of the space coordinates of any point that appears in the image.

Displaying the object

The visibility of edges and faces for any polyhedral (*approximation of space object*) for parallel and central projection can be determined as follows:

The visibility of faces will be checked by

Calculating the angle θ between the view vector \mathbf{v} (in case of central projection, the view vector will be considered as the line connecting camera station S and any vertex) of the face and the normal vector \mathbf{n} of that face. If the angle θ is acute then the face is invisible otherwise it is visible (Figure 9).

So, the dot product can be used to obtain information about the angle between two vectors. Then $\mathbf{v} \cdot \mathbf{n} < 0$ will be characterized as visible faces.

An edge is visible if at least one neighbor face is visible. The edges between one visible and one hidden face are silhouette edges. So, the silhouette is formed by the edges that separate visible from invisible faces on the polyhedron.

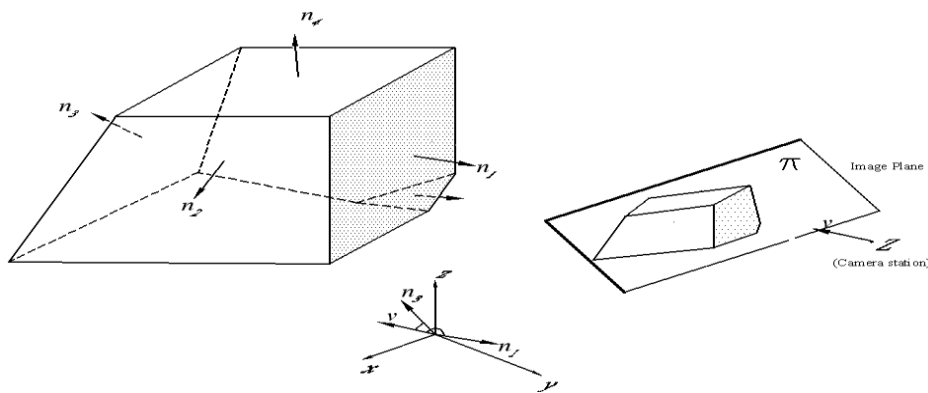


Fig. (9). Perspective Projection of Polyhedron

Calculating the image coordinate of a space point

Let the coordinates of a point $P(x_p, y_p, z_p)$ in space be known relative to xyz - system. Now we want to calculate the image coordinates of point $P^c(x, y)$ (projection of P on π). Let Z be the center of projection with base vector \mathbf{z} and point H (principal point of π) with base vector \mathbf{h} (normal projection of Z on π). Since, point P with base vector \mathbf{p} , its central projection P^c (base vector \mathbf{p}^c) and center of projection Z are collinear, then the base vector of \mathbf{p}^c can be calculated from the following equation:

$$\mathbf{p}^c - \mathbf{z} = \lambda(\mathbf{p} - \mathbf{z}) \quad \lambda \in R$$

To calculate λ , let point P^n (base vector \mathbf{p}^n) be normal projection of P on π as shown in Figure (10). The points P^n , H and P^c lie on one line, which is the normal

projection of the line ZP on π . So, the point P^c divides the two lines ZP and HP^n in the same ratio.

$$\mathbf{p}^c - \mathbf{h} = \lambda(\mathbf{p}^n - \mathbf{h}).$$

The parameter λ can be determined from the following equation $\lambda = \frac{d}{(\mathbf{p} - \mathbf{h}) \cdot \mathbf{s} + d}$

Where \mathbf{s} is unit vector parallel to \overline{ZH} (i.e. normal on image plane π), and d is the distance between Z and H (= focal length)

Choose rectangular coordinate system $o(x, y)$ in plane π with o coinciding with H and y parallel to the projection of z axis on π as shown in Figure (11). Let \mathbf{e}_1 and \mathbf{e}_2 be base vectors located on x and y axes in image plane.

The image coordinates of P^c can be calculated from;

$$x = \lambda(\mathbf{p}^n - \mathbf{h}) \cdot \mathbf{e}_1 = \lambda(\mathbf{p} - \mathbf{h}) \cdot \mathbf{e}_1$$

$$y = \lambda(\mathbf{p}^n - \mathbf{h}) \cdot \mathbf{e}_2 = \lambda(\mathbf{p} - \mathbf{h}) \cdot \mathbf{e}_2$$

The above equation can be rewritten in the following form:

$$x = \frac{x_1}{x_0}, \quad \text{and} \quad y = \frac{x_2}{x_0}, \quad x_0 = \frac{1}{\lambda} = 1 + \frac{(\mathbf{p} - \mathbf{h}) \cdot \mathbf{s}}{d}$$

with $x_1 = (\mathbf{p} - \mathbf{h}) \cdot \mathbf{e}_1$

$$x_2 = (\mathbf{p} - \mathbf{h}) \cdot \mathbf{e}_2$$

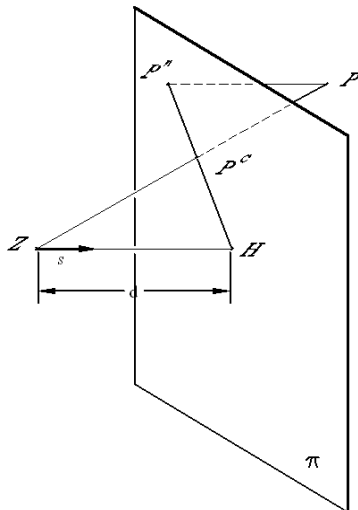


Fig. (10). Central Projection of P

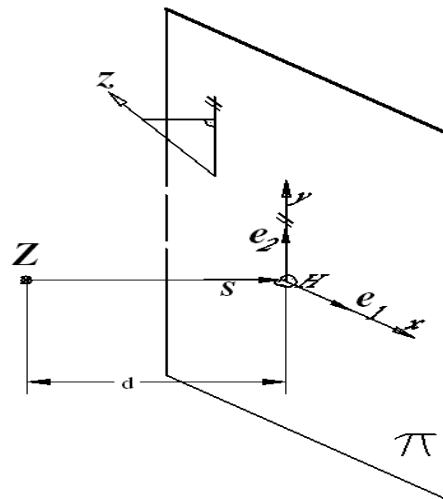


Fig. (11). Image Coordinates System

Calculating space coordinate for image points

Now, how can the space coordinate of any point appear in image plane be determined?

A complete data base is available (*a list of visible faces, a list of vertices whose space and image coordinates are known and a list of edges*). The image of the faces in \mathbf{p} is planer polygon. The relation between the image coordinates of point $P^c(x_0, x_1, x_2)$ and the space coordinates of $P(x_p, y_p, z_p)$ can be presented in a matrix form as:

$$\begin{bmatrix} x_0 \\ x_1 \\ x_2 \end{bmatrix} = \begin{bmatrix} 1 - \frac{\mathbf{h} \cdot \mathbf{s}}{d} & \frac{\mathbf{s}_1}{d} & \frac{\mathbf{s}_2}{d} & \frac{\mathbf{s}_3}{d} \\ -\mathbf{h} \cdot \mathbf{e}_1 & e_{11} & e_{12} & e_{13} \\ -\mathbf{h} \cdot \mathbf{e}_2 & e_{21} & e_{22} & e_{23} \end{bmatrix} \begin{bmatrix} 1 \\ x_p \\ y_p \\ z_p \end{bmatrix}$$

Where $s_1, s_2, s_3, e_{11}, e_{12}, e_{13}$ and e_{21}, e_{22}, e_{23} are components of the vectors $\mathbf{s}, \mathbf{e}_1, \mathbf{e}_2$.

Determination of the face in which P lies.

To determine which face f contains upon point P , it is required to test the image plane whether the point P^c (image of P) lies inside a polygon pl (image of f) or not. To explain this, let the image coordinates of point P^c be given. We consider the following cases:

1. Define the bounding box for the set of vertices of f as shown in Figure (12). A point outside this box cannot be inside the polygon. For the points inside the box, we have:
2. Compute the points of intersection of any line l passing through point P^c with the edges (*considered as line segments but not their extension*) of the polygon. There is always an even number of points of intersection, when a case is avoided when l passes through any vertex. Point P^c separates this set of points into two subsets. Point P^c will be inside the polygon if and only if each subset has an odd numbers of elements.

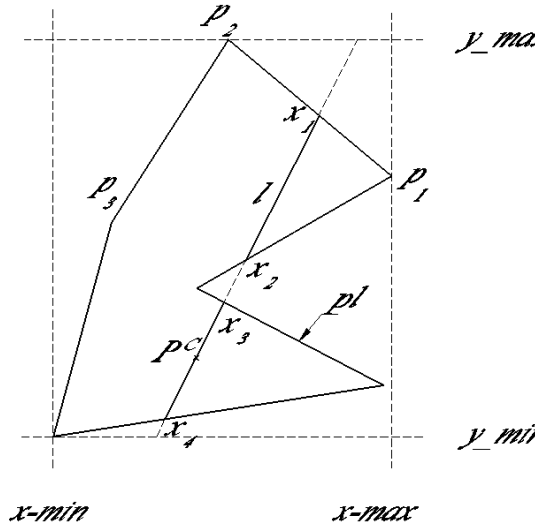


Fig. (12). Relative Position Between Point and Polygon

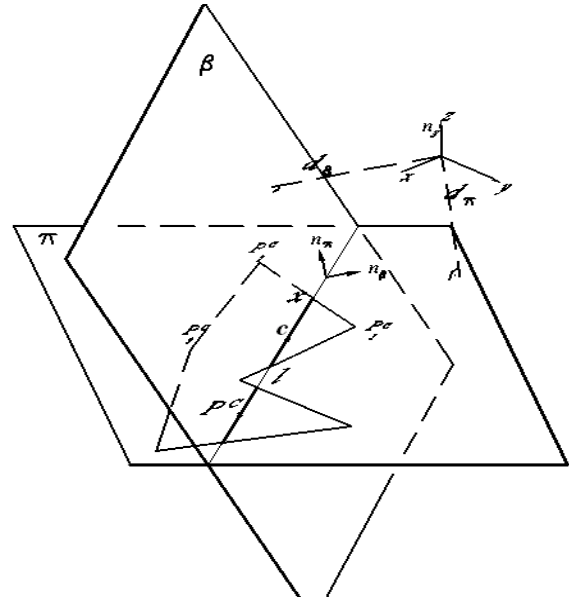


Fig. (13). Intersection of l with Polygon

Finding the points of intersection of l with the loops (Figure 13)

Let l be a line passing through point P^C and a polygon pl in image plane be the image of the visible face f of the object. The position vector \mathbf{x} of can be written in the form:

$$\mathbf{x} = \mathbf{p}^C + \lambda \mathbf{c},$$

where \mathbf{p}^C is the position vector of point P^C and \mathbf{c} is a vector in direction of line l in image plane. From which, $\mathbf{n} \cdot \mathbf{c} = 0$.

So, the computation of \mathbf{x} has been reduced to the computation of any suitable coefficient $\lambda \in R$. After having ordered the values, a sequence of line segments representing the intersection between l and polygon pl will be obtained.

For this reason we introduce the plane \mathbf{b} $\mathbf{n}_\beta \cdot \mathbf{r} = d_\beta$ normal to image plane \mathbf{p} through line l . The equation of plane \mathbf{b} is

$$\mathbf{n}_\beta \cdot \mathbf{r} = d_\beta \text{ Where } \mathbf{n}_\beta = \mathbf{n} \times \mathbf{r} \text{ with } \|\mathbf{r}\| = 1.$$

Where \mathbf{r} is the position vector for any point located in \mathbf{b} , and d_β is the oriented distance between the origin O and plane \mathbf{b} and can be computed with any point $\mathbf{r} = \mathbf{c} \in l$, for any point $P^C \in \pi$ the value $d_p = \mathbf{n}_\beta \cdot \mathbf{p}^C - d_\beta$ gives the oriented distance between P^C and \mathbf{b} .

The following algorithm explains how the points of the intersection between l and pl can be computed. Assuming a certain assumption that the line will not pass through any polygon vertices, then each line segment of pl intersect line l or not must be tested. Supposing that, the test edge has the initial point P_1^C (with base vector \mathbf{p}_1^C) and the end point P_2^C (base vector \mathbf{p}_2^C), the oriented distance $d_{p_1^C}$ and $d_{p_2^C}$ must be used. Then, if the sign of $d_{p_1^C}$ differs from the sign previous $d_{p_2^C}$, the two end points of the test edge are situated on different sides of \mathbf{b} . Then between P_1^C and P_2^C there will be an intersection point x of l with the plane \mathbf{b} . The vector of this point can be expressed as:

$$\mathbf{x} = \frac{1}{d_{p_2^C} - d_{p_1^C}} (d_{p_1^C} \mathbf{p}_1^C - d_{p_2^C} \mathbf{p}_2^C)$$

Conclusion

Documenting historical buildings and the world heritage needs to be done with the ability of measuring all details that appear on the object surfaces. 3D computer model with its real shape and dimensions is the best way of such documentation. Using digital close-range photogrammetric techniques in the form of the digital projector method, 3D computer model of the object with its real shape and dimensions can be easily obtained. Creating 3D computer model animation gives the ability to have a still image for the model from the desired point of view which shows the desired details to be measured. The paused animation determines the camera external orientation according to the frame number. Using the used points in creating the computer model with the paused image, the hidden surfaces' points can be excluded from the system data base. Using the digital close-range photogrammetric techniques with known camera orientations and image coordinates of the points, any point lying on the model's visible surfaces can be calculated. This is a promising new measuring system that will enable photogrammetrists to do their job easily and accurate. The advantage of this system is the ability of measuring any details lying on the computer model surfaces just from a single model image.

References

- [1] Ebrahim M., "Application and evaluation of digital image techniques in close range photogrammetry", *PhD dissertation, Innsbruck University, Austria, 1998.*
- [2] Elsonbaty A and Stachel H., "Generating Solids by Sweeping Polyhedra", *Journal of Geometry and Graphics* Vol. 1, (1997), pp. 13-21.
- [3] Elsonbaty A and Ebrahim M., "A New General Method for Determining 3D Measurements Using Single Image", *International Conference of Geometry and Graphics ICGG*, Vol. 2,(2002), pp 227-231.
- [4] Farin G., "*Curve and Surfaces for Computer Aided Geometric Design*", Academic Press, New York, 1990.
- [5] Hanke K, Ebrahim M, "A General Approach For Object Oriented 3d-Mapping In Digital Close Range Restitution", *International Archives of Photogrammetry and Remote Sensing*, Vol. XXXI, Part B5, Vienna,(1996), p p. 215-219.
- [6] Hanke K, and Ebrahim M., "Monument Presentation Using Digital Architectural Photogrammetry", *CIPA International Symposium, October 1-3, Goteborg, Sweden*
ISPRS, Vol.XXXII, Part 5C1B9, (1997).pp. 401-411.
- [7] Kager, H., Das interaktive Programmsystem ORIENT im Einsatz., *International Archives of Photogrammetry*, Hamburg, Vol. XXIII/5,(1980), pp..390-401.
- [8] Streilein, A., "Videogrammetry and CAAD for Architectural Restitution of Otto-Wagner-Pavillion in Vienna", *Gruen/Kahmen (Eds), Wichmann Verlag, Heidelberg*, (1995) pp. 305-314.
- [9] Waldhäusl, P., "A test object for architectural photogrammetry: Otto Wagner's Underground station "Karlsplatz" in Vienna", *Proceedings of the XIVth International Symposium of CIPA in Delphi*, (1991), pp. 247 - 251.

الإحداثيات الفراغية لتفاصيل نماذج الكمبيوتر باستخدام المساحة التصويرية في المجال المحدود

أحمد أحمد السنباطي (1) - مصطفى عبدالباري ابراهيم (2)

(1) استاذ مشارك بالقسم المدني - كلية الهندسة - جامعة القصيم - المملكة العربية السعودية

(2) استاذ مشارك بالقسم المدني - كلية الهندسة - جامعة أسيوط - جمهورية مصر العربية.

الملخص العربي. فن الرسوم المتحركة للمجسمات الثلاثية الأبعاد قد يكون مفيداً للحصول على الإحداثيات الفراغية للنقاط الواقعة على سطح نماذج الكمبيوتر. تتكون نقاط نماذج الكمبيوتر من فئتين من النقاط: الأولى عبارة عن تلك النقاط التي تم استخدامها لتخليق نموذج الكمبيوتر والتي لها إحداثيات فراغية معلومة. الثانية هي أي نقاط أخرى واقعة على أسطح النموذج وليس لها إحداثيات فراغية معلومة. ان تخليق نماذج الكمبيوتر ثلاثية الأبعاد يمكن أن يتم باستخدام الإحداثيات الفراغية الناتجة من قياسات المساحة التصويرية. بمجرد تخليق نموذج الكمبيوتر، يمكن عمل قياسات مختلفة للنموذج ولكن للنقاط التي تنتمي للفئة الأولى فقط من خلال صورة للنموذج مأخوذة من فيلم حركي له تم تخليقه في برنامج خاص بإنتاج الرسوم المتحركة، أما تلك النقاط التي تنتمي للفئة الثانية فلا يمكن قياس إحداثياتها من هذه الصورة إلا بتوفر شرط إضافي للقياس من صورة مفردة.

والهدف الاساسى لهذا البحث هو كيفية إيجاد الإحداثيات الفراغية لاي نقطة أخرى واقعة على السطح وظاهرة في الصورة (نقاط الفئة الثانية) الملتقطة للمجسم في اي وضع في إطار الفيلم الحركي له. وخلال هذا البحث تم توضيح الفكرة الأساسية واشتقاق المعادلات الرياضية المختلفة لاستنتاج تلك الإحداثيات وهي تعتمد في المقام الأول على الإسقاط المركزى مع تقنيات المساحة التصويرية الرقمية في المجال المحدود. كما تم حل بعض المشاكل التي واجهتنا باستخدام الكمبيوتر جرافيك مثل كيفية تحديد السطح الذي تقع عليه نقطة ما من مجموعة الأسطح التي تظهر في الصورة وكانت الفكرة الأساسية في ذلك هو أولاً تحديد الأسطح الظاهرة والمختفية في نماذج الكمبيوتر وبعدها يتم استبعاد الأسطح المختفية. حالة الأسطح سواء كانت ظاهرة أم مختفية تعتمد على وضع ومكان الصورة الملتقطة للمجسم ثم يلي ذلك تحديد احد هذه الأسطح الظاهرة التي تقع عليها النقطة الفراغية، وبالتالي يمكننا الحصول على الإحداثيات الفراغية لتفاصيل نماذج الكمبيوتر. وخلال هذا البحث سوف يتم شرح ذلك بمزيد من التفاصيل.